

Simultaneous Superconducting and Topological Properties in Mg–Li Electrides at High Pressures

Dan Wang,^{1,2} Hongxing Song,¹ Qidong Hao,^{1,2} Guangfa Yang,¹ Hao Wang,¹ Leilei Zhang,³
Ying Chen,⁴ Xiangrong Chen,^{2*} Huayun Geng^{1,5*}

¹ National Key Laboratory of Shock Wave and Detonation Physics, Institute of Fluid Physics, China
Academy of Engineering Physics, Mianyang, Sichuan 621900, P. R. China;

² Institute of Atomic and Molecular Physics, College of Physics, Sichuan University, Chengdu 610065, P.
R. China;

³ Institute of Nano-Structured Functional Materials, Huanghe Science and Technology College, Zhengzhou
450063, P. R. China;

⁴ Fracture and Reliability Research Institute, School of Engineering, Tohoku University, Sendai 980-8579,
Japan;

⁵ HEDPS, Center for Applied Physics and Technology, and College of Engineering, Peking University,
Beijing 100871, P. R. China.

Abstract:

Electrides as a unique class of emerging materials exhibit fascinating properties and hold important significance for understanding the matter under extreme conditions, which is characterized by valence electrons localized into the interstitial space as quasi-atoms (ISQs). In this work, using crystal structure prediction and first-principles calculations, we identified seven stable phases of Mg-Li that are electride with novel electronic properties under high pressure. Among them, MgLi₁₀ is a semiconductor with a band gap of 0.22 eV; and *Pm-3m* MgLi is superconductor with a superconducting transition temperature of 22.8 K. The important role played by the localization degree of ISQ in the superconducting transition temperature of these electrides is revealed by systematic comparison of Mg-Li with other Li-rich electride superconductors. Furthermore, we proved that *Pm-3m* MgLi and *Pnma* MgLi also have distinct topological behavior with metallic surface states and the non-zero Z_2 invariant. The

* To whom correspondence should be addressed. E-mail: s102genghy@caep.cn; xrchen@scu.edu.cn.

simultaneous coexistence of superconductivity, electronic band topology and electride property in the same structure of *Pm-3m* MgLi and *Pnma* MgLi demonstrates the feasibility of realizing multi-quantum phases in a single material, which will stimulate further research in these interdisciplinary fields.

1 Introduction

The exploration of superconductors is of great interest in condensed matter physics and materials science because of their unique potential value in civil and industrial application¹⁻⁴. Particularly, alkali metals as electrides⁵⁻⁷ exhibit superconductivity which is quite different from hydrogen-rich superconductors^{8,9}. In electrides, the highly-localized electrons in the interstices of the lattice serve as anions, which are known as interstitial quasi-atom (ISQ)¹⁰ and lead to strong core-ISQ polarization, resulting in exotic phenomena such as LA-TA splitting¹¹, universal surface interface metallic states¹², and colossal charge state of impurity atoms⁷. The presence of ISQs also can induce electronic phase transitions from metal to semiconductor, even to insulator, and with possible superconducting phase in them¹³⁻¹⁷.

Recent high-pressure studies indicated that some Li-rich electrides might exhibit superconductivity generally, including Li_5C ¹⁸, Li_5N ¹⁹, Li_6P ²⁰, Li_9Te ²¹, and Li_8As ²², in which it seems ISQs enhance superconductivity. However, in electrides Li_6C ²³ and Li_{10}Se ²⁴, the high superconducting critical temperature is attributed to the strong electron-phonon coupling derived from the synergy of interatomic coupling effect, while ISQs impede superconductivity. On the other hand, ISQs also contribute to the fusion and stability of intermetallic electride superconductors such as Be_2Li ²⁵, LiCa ²⁶, Li_6Al ²⁷, Li_8Cs ²⁸. Recently, in the design of electrides

$\text{Li}_8\text{Au}^{29}$ and $\text{Li}_8\text{H}_4^{30}$, the ISQs are adopted as a feature to achieve diverse topology to improve superconducting temperatures. Overall, the strong charge polarization in electrides provides a versatile tool to tune the electronic structure and superconductivity²². However, the role played by ISQs in superconductivity remains contentious. To establish a clear relation between ISQs and superconductivity is still imperative for to realize high-temperature electride superconductors.

Due to the localization of electron to the interstitial sites to achieve partial independence (i.e., only weakly associated with the nucleus), all insulating and semiconducting electrides are predicted having universal and robust metallic surface or interface states¹², even though some of them might be topologically trivial in terms of conventional topological band structure theory³¹, which indicates electride might have unknown de facto real-space topology that beyond the conventional theories. Nevertheless, some electrides are indeed topological nontrivial in the electronic band structure^{32,33} according to conventional topological band theory. For instance, Ca_3Pb possesses a topologically nontrivial band structure³⁴. In Cs_3O and Ba_5N , the anionic electrons induce an *s-p* band inversion and result in a nontrivial band topology³⁵. Two dimensional electrides Y_2C , Sr_2Bi , and HfBr have also been reported being topological semimetals^{36, 37}. Furthermore, the electride phase of simple metals also display nontrivial semimetallic electronic structure under pressure³⁸. The high-pressure polymorphs of lithium are found to be topological nodal loop semimetals³⁹; the alkali earth metals (Be, Mg, Ca, and Sr) exhibit Dirac nodal line and topological surface states⁴⁰.

In principle, the superconducting and conventional band topological states could be envisioned to emerge in the same electride. Their interplay might lead to interesting properties,

such as the interaction between superconducting surface/edge current and colossal charge states⁷ or the stationary longitudinal acoustic phonon mode^{11, 12}. The search for novel topological superconducting electrider thus is one of the major focuses in material science. As the lightest metallic element, lithium has a rich phase diagram under pressure, and exhibits abundant physicochemical properties^{38, 41, 42}. In addition, its melting behaves like hydrogen (for example, the “U” shape in the melting curve after the melting temperature reaches a maximum⁴³) under compression; but it maintains electrider states that favor superconductivity before entering an semiconducting phase.

In this work, we report seven stable compounds with a wide stoichiometries spanning from 7:1 to 1:10 in Mg-Li system up to 500 GPa. Particularly, *Pm-3m* MgLi and *Pnma* MgLi become superconducting electrideres with a noteworthy T_c of 22.80 K and 8.91 K at high pressure, respectively. By composing and analyzing the variation of superconductivity in typical Li-contained electrider, we obtain a practical relationship between the localization degree of ISQs and T_c , which could be employed as a guide to tune the superconducting temperatures by adjusting the localization of ISQs. Furthermore, it is demonstrated that *Pm-3m* MgLi and *Pnma* MgLi are also topological materials with a nontrivial Z_2 invariant and gapless surface states, thus as the first example of hosting superconductivity and topological nontrivial states in the same electrider at the same time, which provides a platform for exploring the interplay between superconducting, band topological states, and non-nuclear centering of electrons.

2 Computational details

The thermodynamically stable structures of Mg-Li compounds under pressure are explored

by using the ab initio evolutionary algorithm USPEX⁴⁴⁻⁴⁶. Structural optimization and electronic property calculations are performed by using the density functional theory (DFT)^{47, 48} with the projector augmented wave (PAW)⁴⁹ method and the Perdew-Burke-Ernzerhof (PBE) parameterization of the generalized gradient approximation (GGA)⁵⁰ functional as implemented in the Vienna Ab-initio Simulation Package (VASP)^{51, 52}. The energy cutoff for the plane wave basis set is chosen as 700 eV in all calculations. The largest spacing between k-points is set as $2\pi \times 0.015 \text{ \AA}^{-1}$ to generate automatic k-point meshes for the Brillouin zone sampling. All calculations are guaranteed to converge to 10^{-5} eV/atom for energy in the self-consistent field iterations and 0.01 eV/Å for the Hellmann-Feynman forces on atoms, respectively. The $1s^2 2s^1$ and $2s^2 2p^6 3s^2$ electrons are treated in the valence space for Li and Mg, respectively. The Bader charge analysis⁵³ is employed to characterize the charge state of atoms and the charge transfer between atoms and ISQs. Lattice dynamics are calculated by using the small displacement and supercell approach as implemented in our homemade MyPHON code⁵⁴, as well as the open source PHONOPY⁵⁵ code. The formation enthalpy (ΔH) of Mg_mLi_n with respect to the elemental Mg and Li at each pressure is defined as:

$$\Delta H(\text{Mg}_m\text{Li}_n) = [H(\text{Mg}_m\text{Li}_n) - mH(\text{Mg}) - nH(\text{Li})]/(m + n) \quad (1)$$

where H is the enthalpy of the studied compound structure or the most stable elemental reference structure at the given pressure, respectively.

The electron-phonon coupling (EPC) and superconductivity are computed using density functional perturbation theory (DFPT), as implemented in the QUANTUM ESPRESSO (QE) code⁵⁶. The ultrasoft pseudopotential for Li and Mg with a kinetic energy cutoff of 80 Ry are employed. Self-consistent electron density and EPC are calculated by employing carefully

checked different k -meshes and q -meshes: $24 \times 24 \times 24$ k -meshes and $12 \times 12 \times 12$ q -meshes for $Pm-3m$ MgLi, $20 \times 20 \times 20$ k -meshes and $5 \times 5 \times 5$ q -meshes for $Pnma$ MgLi, $16 \times 16 \times 6$ k -meshes and $8 \times 8 \times 3$ q -meshes for $I4/mmm$ Mg₂Li, respectively. The superconducting critical temperature T_c is estimated using the Allen–Dynes-modified McMillan formula^{57, 58} with correction given as follows:

$$T_c = \frac{\omega_{log}}{1.2} \exp \left[-\frac{1.04(1+\lambda)}{\lambda - \mu^*(1+0.62\lambda)} \right] \quad \lambda \leq 1.5 \quad (2)$$

$$T_c = \frac{f_1 f_2 \omega_{log}}{1.2} \exp \left[-\frac{1.04(1+\lambda)}{\lambda - \mu^*(1+0.62\lambda)} \right] \quad \lambda > 1.5 \quad (3)$$

where the effective Coulomb repulsion is taken as $\mu^* = 0.1$. The EPC parameter λ , the logarithmic average frequency ω_{log} , the strong coupling and shape correction factors f_1 and f_2 are:

$$\lambda = 2 \int \frac{\alpha^2 F(\omega)}{\omega} d\omega \quad (4)$$

$$\omega_{log} = \frac{2}{\lambda} \int \frac{\alpha^2 F(\omega) \ln \omega}{\omega} d\omega \quad (5)$$

$$f_1 = \sqrt[3]{1 + \left[\frac{\lambda}{2.46(1+3.8\mu^*)} \right]^{3/2}} \quad (6)$$

$$f_2 = 1 + \frac{\left(\frac{\varpi_2}{\omega_{log}} - 1 \right) \lambda^2}{\lambda^2 + \left[1.82(1+6.3\mu^*) \left(\frac{\varpi_2}{\omega_{log}} \right) \right]^2} \quad (7)$$

$$\varpi_2 = \sqrt{\frac{2}{\lambda} \int \omega \alpha^2 F(\omega) d\omega} \quad (8)$$

Furthermore, using Wannier representations, we also calculate the surface states of the studied compounds using the iterative Green's function as provided in the WANNIERTOOLS package^{59, 60}.

3 Results and discussion

The phase stability of Mg_mLi_n system is investigated by calculating their enthalpy of

formation up to 500 GPa. The compounds located on the convex hull are thermodynamically stable against any type of decomposition. As shown in Fig.1 (a), the predicted convex hulls suggest that Mg-rich compounds are easier to form in a wide range of pressures, while the only Li-rich compound MgLi_{10} with space group $P-1$ is stable up to 118 GPa. Figure 1(b) shows the phase diagram and crystal structure of the stable phases of Mg_mLi_n . The ground-state phase of MgLi is found to be in the CsCl-type⁶¹ structure (space group $Pm-3m$, Pearson symbol cP2) within a pressure range of 0-213 GPa. At higher pressures, MgLi decomposes into Mg_2Li and Li element, as shown in Fig.1(a), Fig.S1(b), and Fig.S2. Interestingly, MgLi becomes the ground state again and is stabilized into the orthorhombic MnP-type⁶² structure (oP8, space group $Pnma$) when between 350 GPa and 500 GPa.

For Mg-rich compositions, Mg_3Li_2 of Os_2Al_3 -type⁶³ and Mg_2Li of MoSi_2 -type⁶⁴ are stable up to 174 GPa and 335 GPa, respectively. Both of them are ordered in a body-centered tetragonal (bct) lattice with space group $I4/mmm$. Mg_3Li crystallizes into the Na_3Cl -type⁶⁵ structure with space group $P4/mmm$ and maintains its stability between 4 GPa and 414 GPa. At elevated pressures, the bct- Mg_4Li becomes stable from 50 to 476 GPa. The structure of Mg_4Li also derives from Os_2Al_3 ⁶³ and crystallizes in the same space group ($I4/mmm$). Their phase diagram at 0 K is summarized in Fig. 1(b).

Furthermore, we also identified several metastable phases based on the fact that their formation enthalpies are not on the convex hull but is very close to it and exhibits dynamical stability (i.e., without any imaginary frequency in the phonon spectrum, see Fig.S3). The corresponding phases are: $P-3m1$ MgLi_2 (170–500 GPa), $Pm-3m$ MgLi (213–250 GPa), $Pnma$ MgLi (315–350 GPa), $I4/mmm$ Mg_3Li_2 (174–300 GPa), $I4/mmm$ Mg_2Li (335–410 GPa),

P4/mmm Mg₃Li (0–4 GPa, 414-500 GPa), *I4/mmm* Mg₄Li (0–50 GPa, 476–500 GPa), and *P4/mmm* Mg₅Li (0–500 GPa).

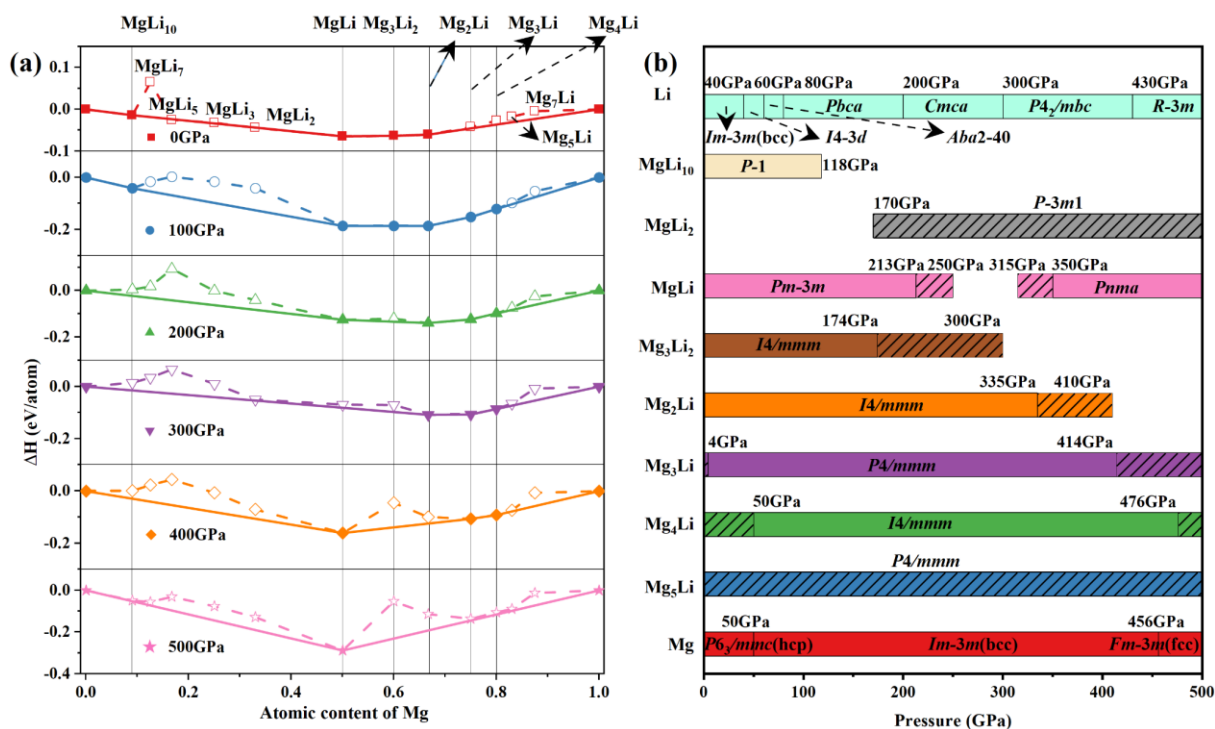


Figure 1. (Color online) Stability of Mg_mLi_n compounds under pressure. (a) Enthalpy of formation of Mg_mLi_n at selected pressures up to 500 GPa, in which the thermodynamically stable compounds are shown in solid symbols, while metastable ones are in open symbols; (b) Predicted phase diagram for stable Mg_mLi_n compounds, where the black slashed regions indicate that the corresponding phases are metastable within the given pressure range. Though that the compounds of MgLi₅, MgLi₃, MgLi₂ at 0 GPa, MgLi₂ at 300 GPa, Mg₅Li at 400 GPa, and MgLi₁₀, Mg₃Li, Mg₄Li, Mg₅Li at 500 GPa are very close to the convex hull (within 3~9 meV/atom), they are denoted as metastable phases here.

As shown in Fig.2 (b), each Li atom in *Pm-3m* MgLi (B2 type structure) is surrounded by eight nearest Mg atoms and six second-nearest Li atoms. The corresponding Li–Li and Li–Mg

distances (2.40 Å and 2.07 Å) are shorter than those in $Pm-3m$ LiAl (2.54 Å and 2.20 Å)⁶⁶ at 200 GPa due to the stronger bonding in the former. In $Pnma$ -MgLi, the Li atoms are bonded to six Mg atoms, with the Li-Mg bond distance of 1.64-1.73 Å at 500 GPa as shown in Fig. S4. On the other hand, the Mg-rich phase can be viewed as a host-guest structure, similar to Li-Al alloys²⁷. The $I4/mmm$ Mg₃Li₂ phase can be considered as the cubic lattice of Li-Mg inserted into the two-layer Mg cubic lattice as a guest. The Li atom is bonded in an eight-coordinated geometry of two inequivalent Mg sites. The first site is $4e$ (0.5, 0.5, 0.68865), and each Mg atom is bonded to eight equivalent Li atoms in a body-centered cubic geometry. The second site is $2a$ (0.0, 0.0, 0.0), and each Mg atom is bonded to four Li atoms. The corresponding Li-Mg distance at 100 GPa is 2.23 Å and 2.26 Å, respectively.

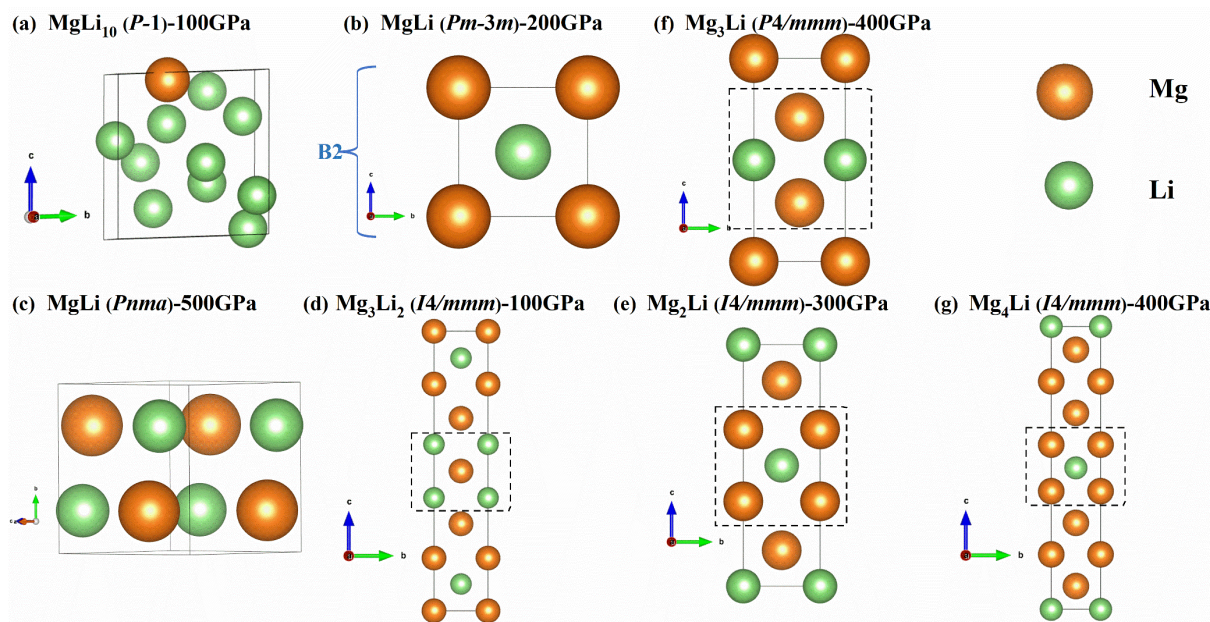


Figure 2. (Color online) Structures of stable Mg_mLi_n compounds under high pressure: (a) $P-1$ MgLi₁₀ at 100 GPa; (b) $Pm-3m$ MgLi at 200 GPa; (c) $Pnma$ MgLi at 500 GPa; (d) $I4/mmm$ Mg₃Li₂ at 100 GPa; (e) $I4/mmm$ Mg₂Li at 300 GPa; (f) $P4/mmm$ Mg₃Li at 400 GPa; (g) $I4/mmm$ Mg₄Li at 400 GPa. Orange and green spheres

represent Mg and Li atoms, respectively.

The structural features of Mg_2Li-I4/mmm , Mg_3Li-P4/mmm , and Mg_4Li-I4/mmm are similar, where each Li atom is coordinated with four Li atoms and eight Mg atoms. In Mg_2Li-I4/mmm phase, the shortest Li–Li and Li–Mg distance at 300 GPa is 2.31 Å and 1.96 Å, respectively. In Mg_3Li-P4/mmm and Mg_4Li-I4/mmm , there are also two inequivalent Mg sites, with the Li–Li, Li–Mg1 and Li–Mg2 bond lengths of 2.22 Å, 1.89 Å, and 2.48 Å at 400 GPa, respectively. The detailed structural information of metastable Mg_mLi_n compounds can be found in Fig.S5 and Table S1 of Supporting Information (SI).

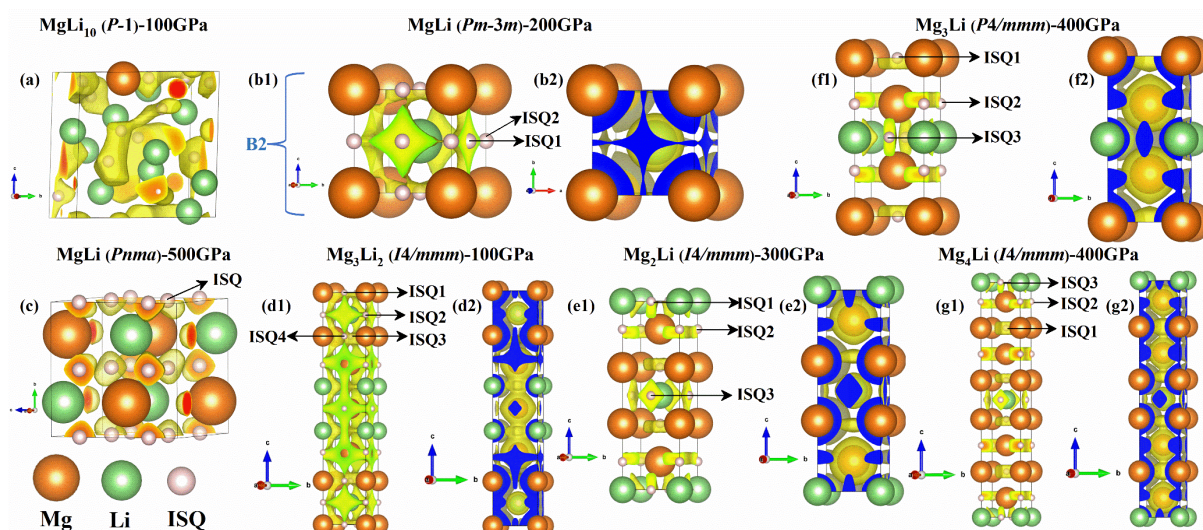


Figure 3. (Color online) Electron localization function (ELF) of Mg_mLi_n : (a) $P-1$ $MgLi_{10}$ at 100 GPa, (isosurface=0.75); (b1) $Pm-3m$ $MgLi$ at 200 GPa, (isosurface=0.60); (c) $Pnma$ $MgLi$ at 500 GPa, (isosurface=0.80); (d1) $I4/mmm$ Mg_3Li_2 at 100 GPa, (isosurface=0.60); (e1) $I4/mmm$ Mg_2Li at 300 GPa, (isosurface=0.65); (f1) $P4/mmm$ Mg_3Li at 400 GPa, (isosurface=0.65); (g1) $I4/mmm$ Mg_4Li at 400 GPa, (isosurface=0.65). Charge density of Mg_mLi_n : (b2) $Pm-3m$ $MgLi$ at 200 GPa, (isosurface=0.0425 e/Bohr³); (d2) $I4/mmm$ Mg_3Li_2 at 100 GPa, (isosurface=0.0325 e/Bohr³); (e2) $I4/mmm$ Mg_2Li at 300 GPa, (isosurface=0.052 e/Bohr³); (f2) $P4/mmm$ Mg_3Li at 400 GPa, (isosurface=0.06 e/Bohr³); (g2) $I4/mmm$ Mg_4Li

at 400 GPa, (isosurface=0.06 e/Bohr³). Orange, green and pink spheres represent Mg atoms, Li atoms and ISQ, respectively. Note that the structures in Fig.2 (b) and (d-g) are all derived from BCC lattice, their ELF as shown in Fig.3(b1) and (d1-g1) are similar to the BCC phase of lithium for the subunit that is of B2 type, and are similar to the uniaxially tensile BCC phase of lithium along *z* direction for those subunits with mixed occupation of atoms other than the B2 type.

The electron localization function (ELF) and charge density are calculated and shown in Fig.3. It is evident that all Mg_{*m*}Li_{*n*} compounds show unambiguous localized interstitial electron, indicating they are indeed electrides according to the “ELF-charge” criterion advocated in Ref. [7]. Moreover, the calculated Bader charge (listed in Table S2 of SI) reveals that the valence states of both Li and Mg atoms are positive, confirming the charge transfer from atomic nuclei to ISQs. In the Li-rich phase (MgLi₁₀), the integrated number of electrons on Li is approximately -0.97 electrons, in other words, with a nominal oxidation state of +1. The localized electrons in interstices mainly come from Li atoms rather than from Mg, since Li has a smaller electronegativity than Mg at 100 GPa⁶⁷. In *Pm-3m* MgLi, the anionic electrons are localized at two non-equivalent octahedral interstitial sites, forming ISQ1 and ISQ2 with a Bader charge of 0.44 e and 0.14 e, respectively. By contrast, the ISQs (with a charge state of 0.92 e) are arranged in layers in *Pnma* MgLi. The *I4/mmm* Mg₃Li₂ is derived from BCC lattice, with its ELF similar to the pristine or uniaxially tensile BCC phase of lithium, depending on whether the corresponding subunit is of the B2 type or not. The averaged Bader charge on the ISQs in this phase is: 0.55 e (ISQ1), 0.64 e (ISQ2), 0.68 e (ISQ3), 0.50 e (ISQ4), respectively. There are three inequivalent interstitial sites in *I4/mmm* Mg₂Li, leading to ISQ1 with 0.64 e,

ISQ2 with 0.84 e, and ISQ3 with 0.64 e, respectively. Excess electrons in both of them are localized in the vertex-sharing octahedral interstitials. The Bader charge analysis of Mg_3Li - $P4/mmm$ gives 1.11 e (ISQ1), 0.89 e (ISQ2), 0.61 e (ISQ3); and 1.15 e (ISQ1), 0.85 e (ISQ2), 0.61 e (ISQ3) for Mg_4Li - $I4/mmm$, respectively.

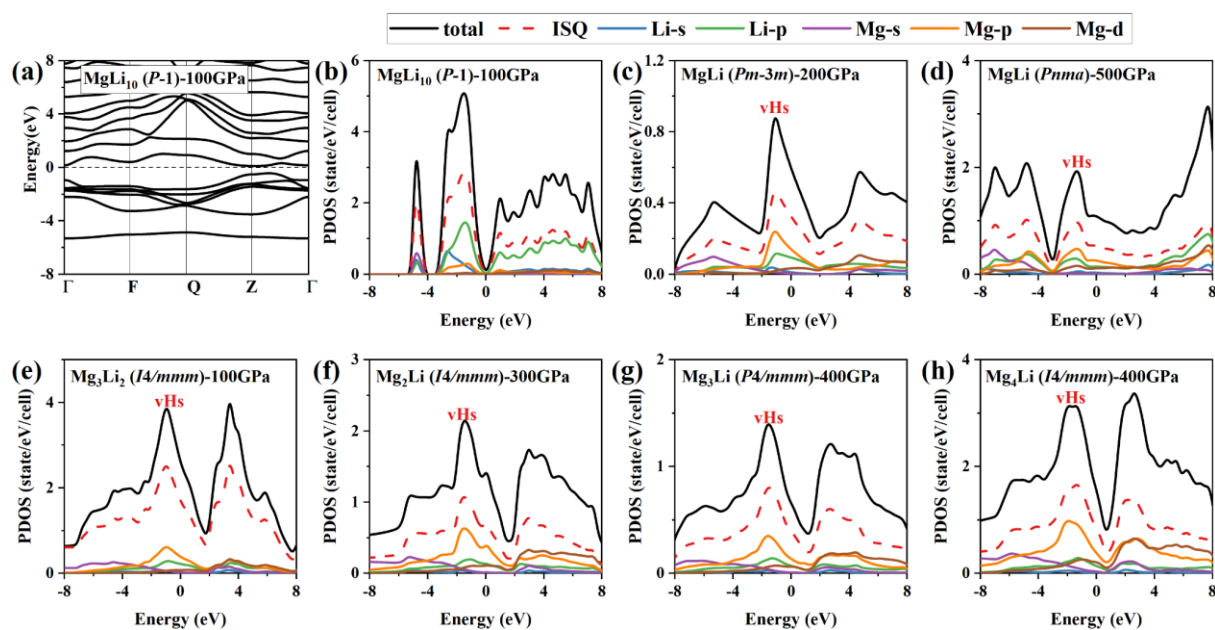


Figure 4. (Color online) (a) Band structure of $P-1$ MgLi_{10} at 100 GPa; PDOS for (b) $P-1$ MgLi_{10} at 100 GPa, (c) $Pm-3m$ MgLi at 200 GPa, (d) $Pnma$ MgLi at 500 GPa, (e) $I4/mmm$ Mg_3Li_2 at 100 GPa, (f) $I4/mmm$ Mg_2Li at 300 GPa, (g) $P4/mmm$ Mg_3Li at 400 GPa, (h) $I4/mmm$ Mg_4Li at 400 GPa, respectively.

Electrides can exhibit interesting electronic properties, such as the semiconducting phases in compressed Li ($C2^{68}$ and $Aba2^{69}$), Na ($hP4^{70}$ and $oP8^{71}$), Li-Na compounds⁷², $\text{Ca}_2\text{N-II}$, $\text{Sr}_2\text{N-II}$, and $\text{Ba}_2\text{N-IV}^{73}$. We thus explored the band structure and projected density of states (PDOS) of the discovered Mg-Li electrides, as shown in Fig. 4. The electride MgLi_{10} is discovered as a semiconductor with an energy gap of 0.08 eV at 60GPa, which increases to 0.22 eV at 100 GPa, as calculated by the revised Heyd-Scuseria-Ernzerhof screened hybrid functional (HSE06). As

shown in Fig.4(b)-(h), the dominant contribution for the DOS at the Fermi level (E_F) comes from the interstitial electron. Moreover, there is not only a strong hybridization between ISQ and the Li-2*p*, Mg-2*p*, and Mg-3*d* electrons, but also remarkable van Hove singularities (vHs) dominated by the anionic electrons near the Fermi level. The increased DOS at the E_F of MgLi and Mg₂Li suggest the possibility of the emergence of superconductivity in such compounds⁷⁴.

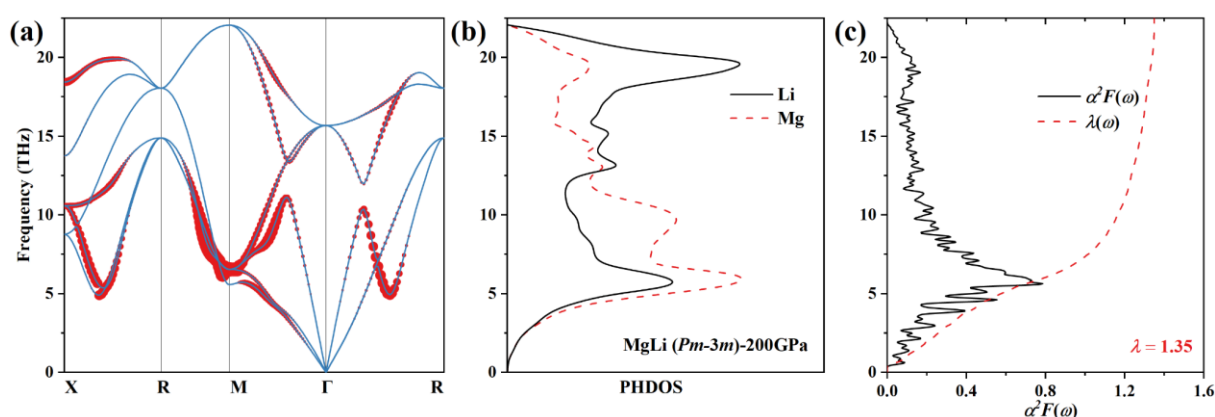


Figure 5. (Color online) (a) Phonon dispersion spectrum, (b) projected phonon density of states (PHDOS), (c) Eliashberg spectral function $\alpha^2F(\omega)$ and electron-phonon coupling constant λ of *Pm-3m* MgLi at 200 GPa, respectively. The size of the solid red circles in (a) is proportional to the electron phonon coupling strength.

To investigate the phonon-mediated superconductivity in Mg-Li alloys, we calculated their phonon dispersion spectra and electron-phonon coupling (EPC) constants λ , as depicted in Figs. 5, S6, S7, and Table 1. Using a Coulomb pseudopotential of $\mu^*= 0.1$, the calculated EPC constant λ of the *Pm-3m* MgLi is around 1.35 at 200 GPa (Fig.5(c)), and the superconductivity critical temperature T_c is estimated to be around 22.80 K. It is worth noting that the main contribution to the superconductivity comes from the low-frequency phonon modes along the R-M- Γ directions (see Fig.5(a), especially at the M point). From the PHDOS and Eliashberg

spectral function, one can determine that the low-frequency region below 13 THz contribute 78.6% to the EPC constant due to the hybridization of the vibrations of Li with Mg atom. The modes at higher frequency contribute 21.4% to the total λ , where the vibration of Li plays a critical role. As for *Pnma* MgLi and *I4/mmm* Mg₂Li, the EPC is weaker, with $\lambda=0.79$ and $\lambda=0.45$, resulting in a $T_c=8.91$ K and $T_c=3.24$ K, respectively. The low-frequency modes of the phonon spectrum also dominate in their total EPC.

Table 1. The calculated total EPC parameter λ , logarithmic average phonon frequency ω_{log} , and superconducting critical temperature T_c of *Pm-3m* MgLi at 200 GPa, *Pnma* MgLi at 500 GPa, and *I4/mmm* Mg₂Li at 300 GPa, respectively.

Phase	Pressure (GPa)	λ	ω_{log}	T_c (K)
<i>Pm-3m</i> MgLi	200 GPa	1.35	174.201	22.80
<i>Pnma</i> MgLi	500 GPa	0.79	176.408	8.91
<i>I4/mmm</i> Mg ₂ Li	300 GPa	0.45	254.768	3.24

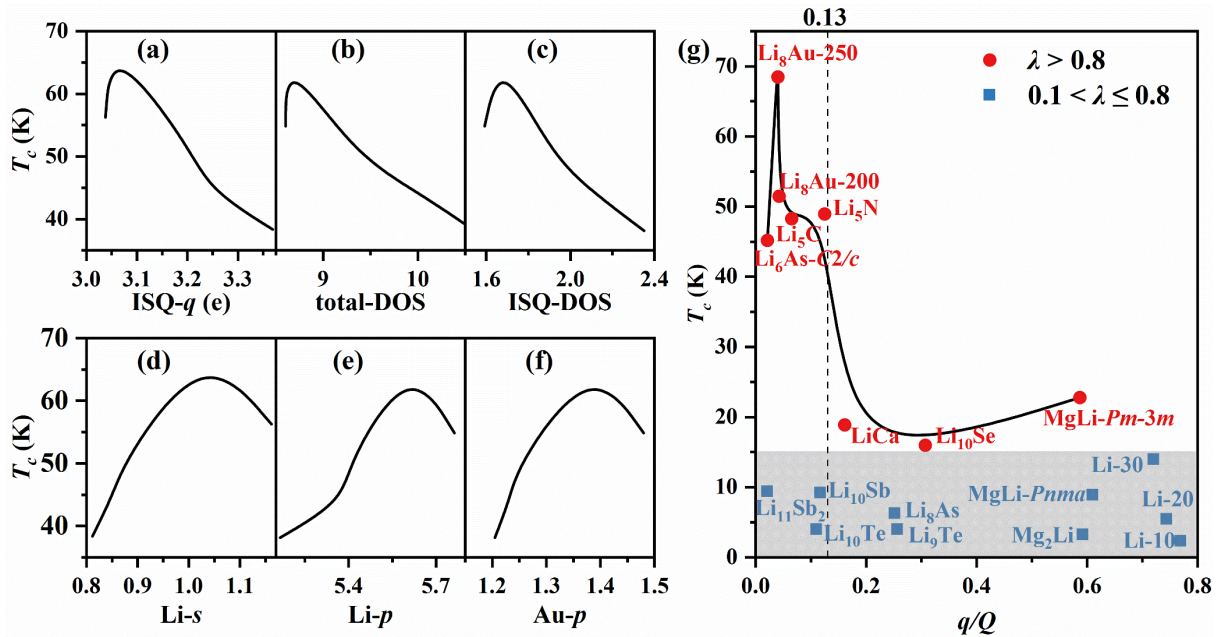


Figure 6. (Color online) The evolution of T_c with (a) the charge of ISQs, (b) the total density of states (DOS)

at the Fermi level, (c) the DOS of ISQs at the Fermi level, (d) the DOS of Li-s orbital at the Fermi level, (e) the DOS of Li-p orbital at the Fermi level, (f) the DOS of Au-p orbital at the Fermi level in Li₈Au, respectively; (g) The evolution of T_c with localization intensity q/Q in typical Li-based electrides. The blue squares represent weakly coupled electrides ($0.1 < \lambda \leq 0.8$), red spheres represent moderately coupled electrides ($\lambda > 0.8$).

As mentioned above, Li-rich compounds exhibit general superconductivity. They in fact can be viewed as variants derived from the elemental Li that is also a superconducting electride. They should have a universal rule that governs the electron localization and superconductivity. To explore this, we took Li₈Au as an example to illustrate the relationship between ISQs and superconductivity, which has the highest T_c reported to date for all electrides. There are two stages as unveiled in Fig. 6(a)-(f): in the first stage (T_c : 55 K \rightarrow 65K), the ISQs enhance the density of states (DOS) at the Fermi level, and the T_c values are positively correlated with the ISQs; In the second stage (T_c : 65 K \rightarrow 40K), the over-localized ISQs start to weaken the electron-phonon coupling, which lowers down the superconducting temperature. The two competing mechanisms result in a maximum critical point which bridges the free-electron gas model of metals to highly localized electrides.

In order to quantify this, let us define the ratio of Bader charge of ISQs (q) and the valence electron (Q) as the localization intensity, and divide the typical electride superconductors into two groups based on EPC constants λ : weakly coupled materials ($0.1 < \lambda \leq 0.8$) and moderately coupled materials ($\lambda > 0.8$). The superconducting critical temperatures of the weakly coupled electrides are below 15K, for which the localization intensity of ISQs hardly affects the superconductivity [see the blue area in Fig. 6(g)]. On the other hand, for the moderately coupled

electrides, the superconducting temperatures increase and then decrease notably and finally become flattened with increasing q/Q . As shown in Fig. 6(g) and Table S3, the localization intensity of ISQs can be used to judge whether the superconducting temperature reaches the optimal value or not. For moderately coupled electrides, the superconductivity can be tuned by adjusting the localization intensity of ISQs. For the Mg-Li system we studied, the $Pm-3m$ MgLi is moderately coupled electride, in which ISQs are over-localized ($q/Q = 0.59$, see the Table S3 in the Supporting Information) thus has a relatively low T_c . In this regard, weakening the localization may increase the superconducting critical temperatures. On the other hand, $Pnma$ MgLi and $I4/mmm$ Mg₂Li are weakly coupled electrides, the localization intensity of ISQs does not affect their T_c .

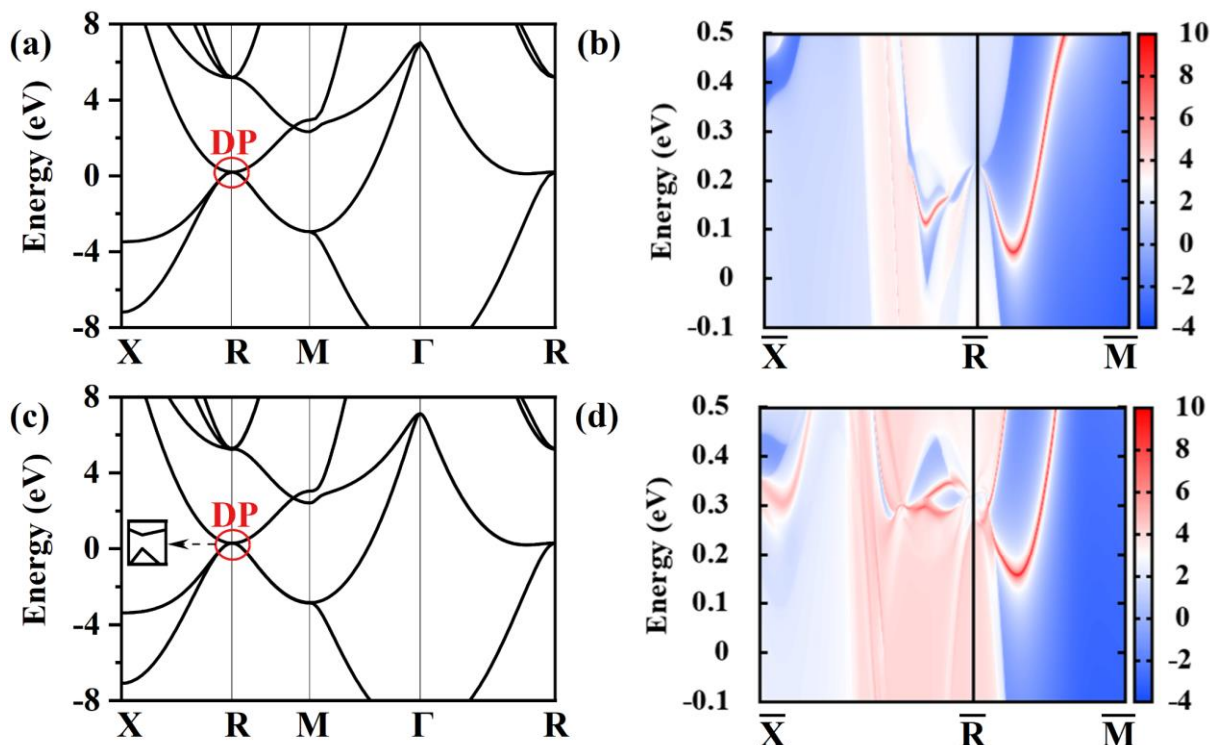


Figure 7. (Color online) (a) Bulk band structure and (b) (001) surface states of $Pm-3m$ MgLi calculated without the SOC effect. (c) Bulk band structure and (d) (001) surface states of $Pm-3m$ MgLi calculated with

the SOC effec. Inset of (c) shows a zoom in of the DP with a small gap opened by SOC. The Fermi level is set to zero. The pressure is 200 GPa.

In the band structure of bulk $Pm-3m$ MgLi, we found that the conduction and valence bands cross each other at the R point, leading to the formation of a band touching point (i.e., a Dirac point). Interestingly, the gapless Dirac point (DP) appears near the Fermi level if without spin-orbit coupling (SOC); whereas the DP becomes gapped when the SOC is turned on. Here, we have investigated its topological properties by studying the surface states (Fig. 7(b)) and the topologically invariant Z_2 indices (Table 2). The latter can be determined from the parity of the wave function at the time reversal invariant momentum (TRIM) points in the presence of time-reversal symmetry and inversion symmetry. The product of the parity for the occupied states at the TRIM points are calculated by $\delta(\mathbf{k}_i) = \prod_{N=1}^{14} \xi_{2N}(\mathbf{k}_i)$, where $\xi_{2N}(\mathbf{k}_i)$ represents the parity of the occupied valence bands at \mathbf{k}_i . The strong topological insulators are characterized by a Z_2 invariant $(\nu_0; \nu_1\nu_2\nu_3) = (1; 111)$. The gapless surface states can be identified near the Fermi level according to the bulk-boundary correspondence. The $Pm-3m$ phase of MgLi electrider thus could be described as a strong topological material, as evidenced by the calculated $Z_2 = (1; 111)$ indices and the nontrivial surface states (Fig.7(d)). For the $Pnma$ phase, the band-crossing point is located at the S point (see Fig. S8) and the gap is also opened up by SOC. The calculated Z_2 invariant (see Table S4 of SI) and metallic surface-states also confirm the nontrivial topological nature of MgLi- $Pnma$. These results indicate that the MgLi electrideres ($Pm-3m$ and $Pnma$) all exhibit topologically nontrivial characteristics. Since superconductivity, band topology and interstitial localization are all derived from the quantum behavior of

electrons. *Pm-3m* MgLi and *Pnma* MgLi demonstrate the multi-quantum state realized in this system.

Table 2. Parity products at TRIMs and the Z_2 indices of *Pm-3m* MgLi at 200 GPa.

TRIM	Parity products	ν	Z_2
X	-	$\nu_1=0, \nu_1'=1$	
3R	+	$\nu_2=0, \nu_2'=1$	
3M	-	$\nu_3=0, \nu_3'=1$	(1;111)
Γ	-	$\nu_0=1$	

Finally, it is worth mentioning that the long-range interaction between atoms and ISQs could lead to an anomalous LA-TA splitting in electrider, analogous to the LO-TO splitting in ionic compounds¹¹. For the isotropic *Pm-3m* MgLi, the magnitude of such splitting is ($\Delta\omega = \omega_{LA} - \omega_{TA}$) 34.5 cm⁻¹ at 200 GPa (see Fig. S10 in the Supporting Information), which might have an impact on the electrical or optical properties of the surface state of this class of materials¹².

4. Conclusion

In summary, we have extensively explored the ground-state structures and phase diagram of Mg-Li system up to 500 GPa by combining crystal structure prediction and first-principles calculations. Seven compounds have been found to be stable, including MgLi₁₀, *Pm-3m* MgLi, *Pnma* MgLi, Mg₃Li₂, Mg₂Li, Mg₃Li, and Mg₄Li, respectively. The Mg-Li system seems to favor Mg-rich compounds compared to the Li-rich side in a wide range of pressures. Remarkably, all high-pressure compounds are electrideres with various morphologies of ISQs.

Calculations of the electronic properties reveal that MgLi_{10} is a semiconductor with almost all of the $2s$ electrons of lithium having been transferred into the interstitial sites. Interestingly, our calculations show that $Pm-3m$ MgLi is a superconductor with a critical temperature T_c of 22.8 K at 200 GPa; and $Pnma$ MgLi and Mg_2Li also manifest superconductivity. We found in the moderately coupled electriles (such as $Pm-3m$ MgLi), the superconducting temperatures increase firstly and then decrease notably and finally become flattened with increasing localization intensity of ISQs. By contrast, in the weakly coupled electriles (such as $Pnma$ MgLi and Mg_2Li), the ISQs hardly affect the superconductivity.

In particular, the valance and conduction bands of MgLi compounds ($Pm-3m$ and $Pnma$) cross each other at the DPs if without SOC; but the gap at the DPs opens up near the Fermi level when with SOC. Both the gapless surface states and the calculated Z_2 invariant clearly confirm that these two phases of MgLi are band topologically nontrivial. The $Pm-3m$ MgLi electrile exhibits both superconductivity and topological behaviors, which also has the highest superconducting T_c among all reported band topological electriles to date. The simultaneous emergence of the superconductivity and the band topology in the same electrile may lead to potential applications in electrile-based quantum devices.

Author contributions

Dan Wang: Investigation, Methodology, Writing - original draft, Writing - review & editing. Hong X. Song: Methodology, Writing - review & editing. Qi D. Hao: Methodology, Writing - review & editing. Guang F. Yang: Methodology, Writing - review & editing. Hao Wang: Methodology. Lei L. Zhang: Writing - review & editing. Xiang R. Chen: Supervision, Project

administration. Hua Y. Geng: Idea conceiving, Project design, Writing, Reviewing, and Editing, Supervision, Project administration, Software.

Conflicts of interest

The authors declare no competing interests.

Data availability

All data are included in the manuscript and supporting information.

Code availability

The VASP code used in this paper is commercial software provided by VASP Software GmbH. All others are open-source codes that can be obtained via internet.

Supporting Information

The Enthalpy difference for different Ecut; The enthalpy of formation, calculated phonon spectra, and histogram of interatomic separations of Mg_mLi_n ; The structure of $P-3m1$ $MgLi_2$ and $P4/mmm$ Mg_5Li ; The structure information of Mg_mLi_n ; The valence state of Mg and Li atoms and the Bader charge of ISQs in Mg_mLi_n compounds. The phonon dispersion relations, PHDOS, $\alpha^2F(\omega)$ and EPC parameter λ of $Pnma$ $MgLi$ and $I4/mmm$ Mg_2Li ; The charge state of ISQs(q), valence electrons(Q), q/Q , EPC parameter λ , and superconducting critical temperature T_c of typical electrides that contain Li; The topological behaviors of $MgLi-Pnma$; Band structures of $I4/mmm$ Mg_3Li_2 , $I4/mmm$ Mg_2Li , $P4/mmm$ Mg_3Li , and $I4/mmm$ Mg_4Li ; LA-TA splitting of $Pm-3m$ $MgLi$.

Acknowledgments

This work was supported by the National Key R&D Program of China under Grant No.

2021YFB3802300, the Foundation of National key Laboratory of shock wave and detonation physics (No. 2023JCJQLB05401), the National Natural Science Foundation of China under Grant No. 12074274, and the NSAF under Grant No. U1730248. Part of the computation was performed using the supercomputer at the Center for Computational Materials Science (CCMS) of the Institute for Materials Research (IMR) at Tohoku University, Japan.

References

1. Ashcroft, N. W., Metallic hydrogen: a high-temperature superconductor? *Phys. Rev. Lett.* **1968**, *21* (26), 1748.
2. Drozdov, A. P.; Eremets, M. I.; Troyan, I. A.; Ksenofontov, V.; Shylin, S. I., Conventional superconductivity at 203 kelvin at high pressures in the sulfur hydride system. *Nature* **2015**, *525* (7567), 73-76.
3. Somayazulu, M.; Ahart, M.; Mishra, A. K.; Geballe, Z. M.; Baldini, M.; Meng, Y.; Struzhkin, V. V.; Hemley, R. J., Evidence for superconductivity above 260 K in lanthanum superhydride at megabar pressures. *Phys. Rev. Lett.* **2019**, *122* (2), 027001.
4. Sun, Y.; Lv, J.; Xie, Y.; Liu, H.; Ma, Y., Route to a superconducting phase above room temperature in electron-doped hydride compounds under high pressure. *Phys. Rev. Lett.* **2019**, *123* (9), 097001.
5. Bergara, A.; Neaton, J. B.; Ashcroft, N. W., Pairing, π -bonding, and the role of nonlocality in a dense lithium monolayer. *Phys. Rev. B* **2000**, *62* (12), 8494.
6. Rodriguez-Prieto, A.; Bergara, A., Pressure induced complexity in a lithium monolayer: Ab initio calculations. *Phys. Rev. B* **2005**, *72* (12), 125406.
7. Zhang, L. L.; Wu, Q.; Li, S. R.; Sun, Y.; Yan, X. Z.; Chen, Y.; Geng, H. Y., Interplay of anionic quasi-atoms and interstitial point defects in electrified: abnormal interstice occupation and colossal charge state of point defects in dense fcc-Lithium. *ACS Appl. Mater. Interfaces* **2021**, *13* (5), 6130-6139.
8. Struzhkin, V. V.; Eremets, M. I.; Gan, W.; Mao, H. K.; Hemley, R. J., Superconductivity in dense lithium. *Science* **2002**, *298* (5596), 1213-1215.
9. Shimizu, K.; Ishikawa, H.; Takao, D.; Yagi, T.; Amaya, K., Superconductivity in compressed lithium at 20 K. *Nature* **2002**, *419* (6907), 597-599.

10. Miao, M. S.; Hoffmann, R., High pressure electrides: a predictive chemical and physical theory. *Acc. Chem. Res.* **2014**, *47* (4), 1311-1317.
11. Zhang, L. L.; Geng, H. Y.; Wu, Q., Prediction of anomalous LA-TA splitting in electrides. *Matter Radiat. Extremes* **2021**, *6* (3), 038403.
12. Wang, D.; Song, H.; Zhang, L.; Wang, H.; Sun, Y.; Wu, F.; Chen, Y.; Chen, X.; Geng, H., Universal metallic surface states in electrides. *J. Phys. Chem. C* **2024**, *128* (4), 1845-1854.
13. Marques, M.; McMahon, M. I.; Gregoryanz, E.; Hanfland, M.; Guillaume, C. L.; Pickard, C. J.; Ackland, G. J.; Nelmes, R. J., Crystal structures of dense lithium: a metal-semiconductor-metal transition. *Phys. Rev. Lett.* **2011**, *106* (9), 095502.
14. Lv, B.; Zhu, X. Y.; Lorenz, B.; Wei, F. Y.; Xue, Y. Y.; Yin, Z. P.; Kotliar, G.; Chu, C. W., Superconductivity in the Mn_5Si_3 -type Zr_5Sb_3 system. *Phys. Rev. B* **2013**, *88* (13), 134520.
15. Ge, Y.; Guan, S.; Liu, Y., Two dimensional superconductors in electrides. *New J. Phys.* **2017**, *19* (12), 123020.
16. Miyakawa, M.; Kim, S. W.; Hirano, M.; Kohama, Y.; Kawaji, H.; Atake, T.; Ikegami, H.; Kono, K.; Hosono, H., Superconductivity in an inorganic electride $12CaO \cdot 7Al_2O_3 \cdot e^-$. *J. Am. Chem. Soc.* **2007**, *129* (23), 7270-7271.
17. Hosono, H.; Kitano, M., Advances in materials and applications of inorganic electrides. *Chem. Rev.* **2021**, *121* (5), 3121-3185.
18. Pereira, Z. S.; Faccin, G. M.; Silva, E. Z. D., Predicted superconductivity in the electride Li_5C . *J. Phys. Chem. C* **2021**, *125* (16), 8899-8906.
19. Wan, Z.; Zhang, C.; Yang, T.; Xu, W.; Zhang, R., Predicted superconductivity and superionic state in the electride Li_5N under high pressure. *New J. Phys.* **2022**, *24* (11), 113012.
20. Zhao, Z.; Zhang, S.; Yu, T.; Xu, H.; Bergara, A.; Yang, G., Predicted pressure-induced superconducting transition in electride Li_6P . *Phys. Rev. Lett.* **2019**, *122* (9), 097002.
21. Zhang, X.; Li, F.; Bergara, A.; Yang, G., Pressure-induced superconductivity in Li-Te electrides. *Phys. Rev. B* **2021**, *104* (13), 134505.
22. Zhao, Y.; Bergara, A.; Zhang, X.; Li, F.; Liu, Y.; Yang, G., Interstitial anionic electrons favoring superconductivity in Li-As electrides. *Phys. Rev. B* **2023**, *108* (10), 104505.
23. Liu, Z.; Zhuang, Q.; Tian, F.; Duan, D.; Song, H.; Zhang, Z.; Li, F.; Li, H.; Li, D.; Cui, T.,

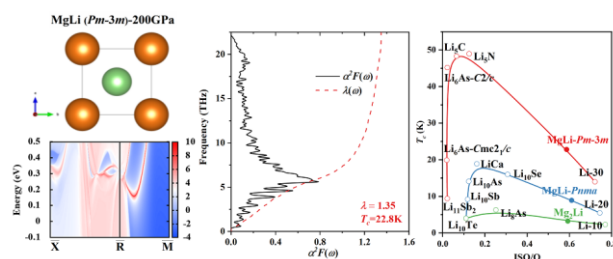
- Proposed superconducting electride Li_6C by sp-hybridized cage states at moderate pressures. *Phys. Rev. Lett.* **2021**, *127* (15), 157002.
24. Zhang, X.; Zhao, Y.; Bergara, A.; Yang, G., Superconducting Li_{10}Se electride under pressure. *J. Chem. Phys.* **2022**, *156* (19), 194112.
25. Errea, I.; Martinez-Canales, M.; Bergara, A., *Ab initio study* of superconducting hexagonal Be_2Li under pressure. *Phys. Rev. B* **2008**, *78* (17), 172501.
26. Xu, Y.; Chen, C.; Wang, S.; Sun, X., Novel structures and superconductivities of calcium–lithium alloys at high pressures: A first-principles study. *J. Alloy. Compd.* **2016**, *669*, 101-107.
27. Wang, X.; Wang, Y.; Wang, J.; Pan, S.; Lu, Q.; Wang, H. T.; Xing, D.; Sun, J., Pressure stabilized lithium-aluminum compounds with both superconducting and superionic behaviors. *Phys. Rev. Lett.* **2022**, *129* (24), 246403.
28. Huang, H. M.; Zhu, Q.; Blatov, V. A.; Oganov, A. R.; Wei, X.; Jiang, P.; Li, Y. L., Novel topological motifs and superconductivity in Li-Cs system. *Nano Lett.* **2023**, *23* (11), 5012-5018.
29. Zhang, X. G.; Yao, Y. S.; Ding, S. C.; Bergara, A.; Li, F.; Liu, Y.; Zhou, X. F.; Yang, G. C., Superconductivity in Li_8Au electride. *Phys. Rev. B* **2023**, *107* (10), L100501.
30. Guo, Z.; Bergara, A.; Zhang, X.; Li, X.; Ding, S.; Yang, G., Superconductivity in Li_8H_n electrides: The effect of interstitial anionic electrons on electron-phonon coupling. *Phys. Rev. B* **2024**, *109* (13), 134505.
31. Xu, Y.; Elcoro, L.; Li, G.; Song, Z. D.; Regnault, N.; Yang, Q.; Sun, Y.; Parkin, S.; Felser, C.; Bernevig, B. A., Three-dimensional real space invariants, obstructed atomic insulators and a new principle for active catalytic sites. *arXiv* **2021**, *2111*, 02433.
32. Liu, C.; Nikolaev, S. A.; Ren, W.; Burton, L. A., Electrides: a review. *J. Mater. Chem. C* **2020**, *8* (31), 10551-10567.
33. Meng, W.; Zhang, X.; Jiang, J.; Li, Z.; Liu, Y.; Dai, X.; Liu, G., Multi-Dimensional Topological Fermions in Electrides. *Adv. Phys. Res.* **2023**, *2* (7), 2200119.
34. Zhang, X.; Guo, R.; Jin, L.; Dai, X.; Liu, G., Intermetallic Ca_3Pb : a topological zero-dimensional electride material. *J. Mater. Chem. C* **2018**, *6* (3), 575-581.
35. Park, C.; Kim, S. W.; Yoon, M., First-principles prediction of new electrides with nontrivial band topology based on one-Dimensional building blocks. *Phys. Rev. Lett.* **2018**, *120* (2), 026401.
36. Zhang, X.; Xiao, Z.; Lei, H.; Toda, Y.; Matsuishi, S.; Kamiya, T.; Ueda, S.; Hosono, H., Two-

- dimensional transition-metal electride Y_2C . *Chem. Mater.* **2014**, *26* (22), 6638-6643.
37. Huang, H.; Jin, K. H.; Zhang, S.; Liu, F., Topological electride Y_2C . *Nano Lett.* **2018**, *18* (3), 1972-1977.
38. Mack, S. A.; Griffin, S. M.; Neaton, J. B., Emergence of topological electronic phases in elemental lithium under pressure. *Proc. Natl. Acad. Sci. U. S. A.* **2019**, *116* (19), 9197-9201.
39. Elatresh, S. F.; Zhou, Z.; Ashcroft, N. W.; Bonev, S. A.; Feng, J.; Hoffmann, R., High-pressure lithium as an elemental topological semimetal. *Phys. Rev. Mater.* **2019**, *3* (4), 044203.
40. Li, R.; Ma, H.; Cheng, X.; Wang, S.; Li, D.; Zhang, Z.; Li, Y.; Chen, X. Q., Dirac node lines in pure alkali earth metals. *Phys. Rev. Lett.* **2016**, *117* (9), 096401.
41. Deemyad, S.; Schilling, J. S., Superconducting phase diagram of Li metal in nearly hydrostatic pressures up to 67 GPa. *Phys. Rev. Lett.* **2003**, *91* (16), 167001.
42. Yu, Z.; Geng, H. Y.; Sun, Y.; Chen, Y., Optical properties of dense lithium in electride phases by first-principles calculations. *Sci. Rep.* **2018**, *8* (1), 3868.
43. Geng, H. Y.; Wu, Q., Predicted reentrant melting of dense hydrogen at ultra-high pressures. *Sci. Rep.* **2016**, *6*, 36745.
44. Oganov, A. R.; Glass, C. W., Crystal structure prediction using ab initio evolutionary techniques: principles and applications. *J. Chem. Phys.* **2006**, *124* (24), 244704.
45. Oganov, A. R.; Lyakhov, A. O.; Valle, M., How evolutionary crystal structure prediction works--and why. *Acc. Chem. Res.* **2011**, *44* (3), 227-237.
46. Lyakhov, A. O.; Oganov, A. R.; Stokes, H. T.; Zhu, Q., New developments in evolutionary structure prediction algorithm USPEX. *Comput. Phys. Commun.* **2013**, *184* (4), 1172-1182.
47. Kohn, W.; Sham, L. J., Quantum density oscillations in an inhomogeneous electron gas. *Phys. Rev.* **1965**, *137* (6A), 1697-1705.
48. Hohenberg, P.; Kohn, W., Inhomogeneous electron gas. *Phys. Rev.* **1964**, *136* (3), B864.
49. Blochl, P. E., Projector augmented-wave method. *Phys. Rev. B Condens. Matter.* **1994**, *50* (24), 17953-17979.
50. Perdew, J. P.; Burke, K.; Ernzerhof, M., Generalized gradient approximation made simple. *Phys. Rev. Lett.* **1996**, *77* (18), 3865.
51. Kresse, G.; Furthmüller, J., Efficient iterative schemes for ab initio total-energy calculations using a plane-wave basis set. *Phys. Rev. B* **1996**, *54* (16), 11169.
52. Kresse, G.; Furthmüller, J., Efficiency of ab-initio total energy calculations for metals and semiconductors

- using a plane-wave basis set. *Comp. Mater. Sci.* **1996**, *6* (1), 15-50.
53. Yu, M.; Trinkle, D. R., Accurate and efficient algorithm for Bader charge integration. *J. Chem. Phys.* **2011**, *134* (6), 064111.
54. Geng, H. Y., Full Temperature-Dependent Potential and Anharmonicity in Metallic Hydrogen: Colossal NQE and the Consequences. *J Phys. Chem. C* **2022**, *126* (45), 19355-19366.
55. Togo, A.; Tanaka, I., First principles phonon calculations in materials science. *Scripta Mater.* **2015**, *108*, 1-5.
56. Giannozzi, P.; Baroni, S.; Bonini, N.; Calandra, M.; Car, R.; Cavazzoni, C.; Ceresoli, D.; Chiarotti, G. L.; Cococcioni, M.; Dabo, I.; et al., QUANTUM ESPRESSO: a modular and open-source software project for quantum simulations of materials. *J. Phys.: Condens. Matt.* **2009**, *21* (39), 395502.
57. Dynes, R. C., McMillan's equation and the T_c of superconductors. *Solid State Commun.* **1972**, *10* (7), 615-618.
58. Allen, P. B.; Dynes, R. C., Transition temperature of strong-coupled superconductors reanalyzed. *Phys. Rev. B* **1975**, *12* (3), 905.
59. Sancho, M. P. L.; Sancho, J. M. L.; Rubio, J., Highly convergent schemes for the calculation of bulk and surface Green functions. *J. Phys. F: Met. Phys.* **1985**, *15* (4), 851-858.
60. Wu, Q.; Zhang, S.; Song, H. F.; Troyer, M.; Soluyanov, A. A., WannierTools: An open-source software package for novel topological materials. *Comput. Phys. Commun.* **2018**, *224*, 405-416.
61. Ganesan, V.; Girirajan, K. S., Lattice parameter and thermal expansion of CsCl and CsBr by x-ray powder diffraction. *Pramana* **1986**, *27* (3), 475-478.
62. Rundqvist, S.; Nawapong, P. C.; Widmark, G.; Nielsen, P. H.; Sjöberg, B.; Larsen, E., Crystal structure refinements of some MnP-type phosphides. *Acta Chem. Scand.* **1965**, *19* (19), 1006-1008.
63. Edshammar, L. E.; Longo, J. M.; Marinder, B. O.; Nielsen, P. H.; Sjöberg, B.; Larsen, E., The crystal structures of Os₂Al₃ and OsAl₂. *Acta Chem. Scand.* **1965**, *19* (19), 871-874.
64. Harada, Y.; Morinaga, M.; Saso, D.; Takata, M.; Sakata, M., Refinement in crystal structure of MoSi₂. *Intermetallics* **1998**, *6* (6), 523-527.
65. Zhang, W.; Oganov, A. R.; Goncharov, A. F.; Zhu, Q.; Boulfelfel, S. E.; Lyakhov, A. O.; Stavrou, E.; Somayazulu, M.; Prakapenka, V. B.; Konopkova, Z., Unexpected stable stoichiometries of sodium chlorides. *Science* **2013**, *342* (6165), 1502-1505.
66. Li, C.; Yang, W.; Sheng, H. W., Bridge-bond formation in aluminum and its alloys under high pressure.

Phys. Rev. Mater. **2022**, 6 (3), 033601

67. Dong, X.; Oganov, A. R.; Cui, H.; Zhou, X. F.; Wang, H. T., Electronegativity and chemical hardness of elements under pressure. *Proc. Natl. Acad. Sci. U. S. A.* **2022**, 119 (10), e2117416119.
68. Yao, Y.; Tse, J. S.; Klug, D. D., Structures of insulating phases of dense lithium. *Phys. Rev. Lett.* **2009**, 102 (11), 115503.
69. Miao, M. S.; Hoffmann, R.; Botana, J.; Naumov, I. I.; Hemley, R. J., Quasimolecules in compressed Lithium. *Angew. Chem. Int. Ed. Engl.* **2017**, 56 (4), 972-975.
70. Ma, Y.; Eremets, M.; Oganov, A. R.; Xie, Y.; Trojan, I.; Medvedev, S.; Lyakhov, A. O.; Valle, M.; Prakapenka, V., Transparent dense sodium. *Nature* **2009**, 458 (7235), 182-185.
71. Li, Y.; Wang, Y.; Pickard, C. J.; Needs, R. J.; Wang, Y.; Ma, Y., Metallic icosahedron phase of sodium at terapascal pressures. *Phys. Rev. Lett.* **2015**, 114 (12), 125501.
72. Chen, Y. M.; Geng, H. Y.; Yan, X. Z.; Wang, Z. W.; Chen, X. R.; Wu, Q., Predicted novel insulating electrider compound between alkali metals lithium and sodium under high pressure. *Chin. Phys. B* **2017**, 26 (5), 056102.
73. Zhang, Y.; Wu, W.; Wang, Y.; Yang, S. A.; Ma, Y., Pressure-stabilized semiconducting electrides in alkaline-earth-metal subnitrides. *J. Am. Chem. Soc.* **2017**, 139 (39), 13798-13803.
74. Quan, Y.; Pickett, W. E., Van Hove singularities and spectral smearing in high-temperature superconducting H₃S. *Phys. Rev. B* **2016**, 93 (10), 104526.



TOC Graphic

Supporting Information for

Superconducting and Topological Properties in Mg–Li Electrides at High Pressures

Dan Wang,^{1,2} Hong X. Song,¹ Qi D. Hao,^{1,2} Guang F. Yang,¹ Hao Wang,¹ Lei L. Zhang,³
Ying Chen,⁴ Xiang R. Chen,^{2*} Hua Y. Geng^{1,5*}

¹ *National Key Laboratory of Shock Wave and Detonation Physics, Institute of Fluid Physics, China
Academy of Engineering Physics, Mianyang, Sichuan 621900, P. R. China;*

² *Institute of Atomic and Molecular Physics, College of Physics, Sichuan University, Chengdu 610065, P.
R. China;*

³ *Institute of Nano-Structured Functional Materials, Huanghe Science and Technology College, Zhengzhou
450063, P. R. China;*

⁴ *Fracture and Reliability Research Institute, School of Engineering, Tohoku University, Sendai 980-8579,
Japan;*

⁵ *HEDPS, Center for Applied Physics and Technology, and College of Engineering, Peking University,
Beijing 100871, P. R. China.*

* To whom correspondence should be addressed. E-mail: s102genghy@caep.cn; xrchen@scu.edu.cn.

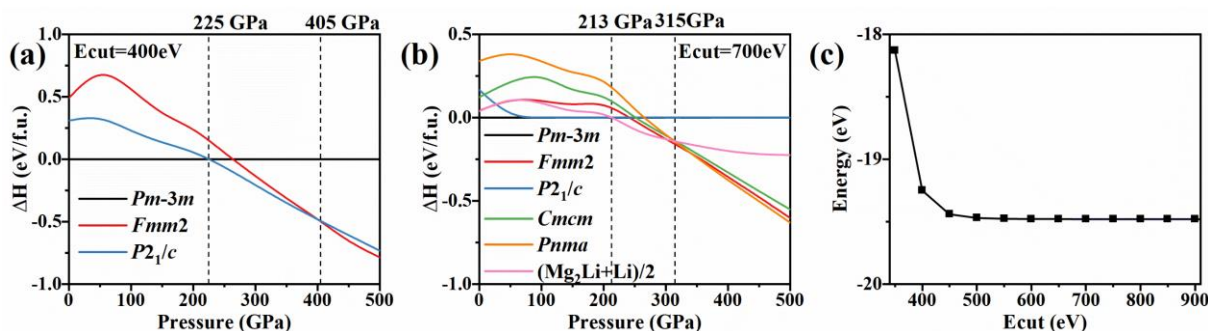


Figure S1. (Color online) (a) Enthalpy difference of MgLi in $Fmm2$ and $P2_1/c$ phases with respect to the $Pm-3m$ phase for E_{cut} : 400 eV; The dashed-lines indicate the pressure of the phase transition; (b) Enthalpy difference of MgLi in $Fmm2$, $P2_1/c$, $Cmcm$, and $Pnma$ phases with respect to the $Pm-3m$ phase for E_{cut} : 700 eV; (c) Convergence test for the energy cutoff (E_{cut}) of the plane wave basis.

As shown in Fig.S1, the $Pm-3m$ MgLi transforms to the $P2_1/c$ phase at 225 GPa and then transforms to the $Fmm2$ phase at 405 GPa if with a cut-off energy of 400 eV, which are consistent with the results of the previous theoretical study¹. However, when the cut-off energy for the plane-wave basis is increased to 700 eV, the picture is changed: $Pm-3m$ MgLi decomposes into Mg_2Li and Li at 213 GPa and then becomes stable again into the $Pnma$ phase at 315 GPa. Based on the convergence test for the energy cutoff of plane wave basis, the results of E_{cut} : 700 eV are more reliable.

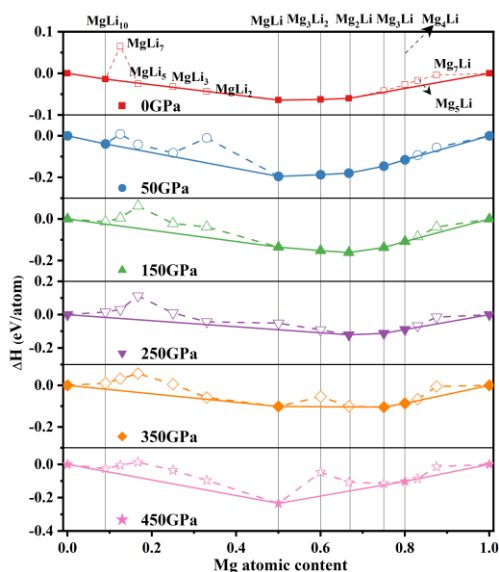


Figure S2. (Color online) Enthalpy of formation of Mg_mLi_n under 0 GPa, 50 GPa, 150 GPa, 250 GPa, 350 GPa, and 450 GPa. The thermodynamically stable compounds are shown by solid symbols.

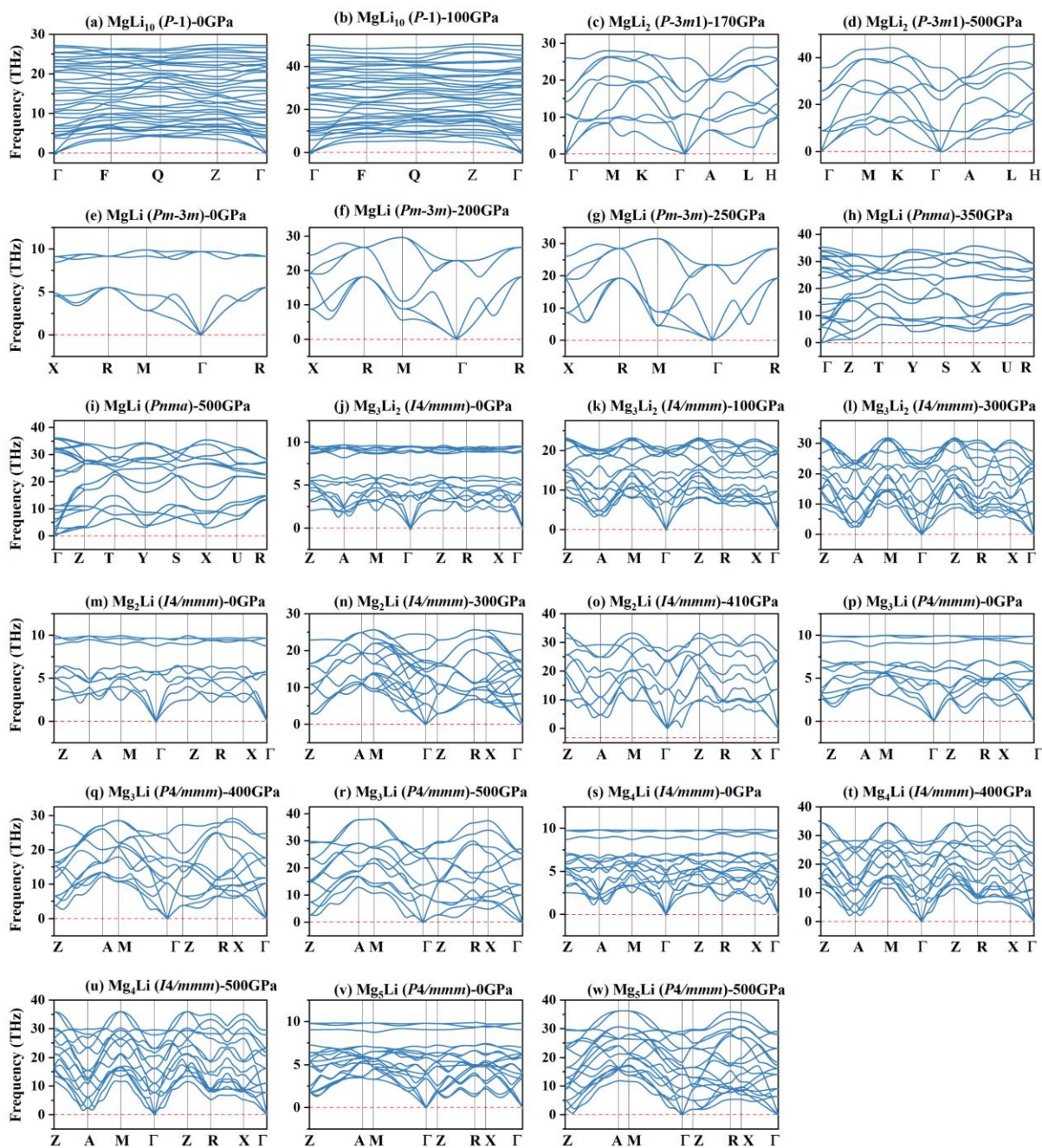


Figure S3. (Color online) Calculated phonon spectra of $P-1$ $MgLi_{10}$ at (a) 0 GPa and (b) 100 GPa; Calculated phonon spectra of $P-3m1$ $MgLi_2$ at (c) 170 GPa and (d) 500 GPa; Calculated phonon spectra of $Pm-3m$ $MgLi$ at (e) 0 GPa, (f) 200 GPa, and (g) 250 GPa; Calculated phonon spectra of $Pnma$ $MgLi$ at (h) 350 GPa, (i) 500 GPa; Calculated phonon spectra of $I4/mmm$ Mg_3Li_2 at (j) 0 GPa, (k) 100 GPa, and (l) 300 GPa; Calculated

phonon spectra of $I4/mmm$ Mg_2Li at (m) 0 GPa, (n) 300 GPa, and (o) 410 GPa; Calculated phonon spectra of $P4/mmm$ Mg_3Li at (p) 0 GPa, (q) 400 GPa, and (r) 500 GPa; Calculated phonon spectra of $I4/mmm$ Mg_4Li at (s) 0 GPa, (t) 400 GPa, and (u) 500 GPa; Calculated phonon spectra of $P4/mmm$ Mg_5Li at (v) 0 GPa and (w) 500 GPa, respectively.

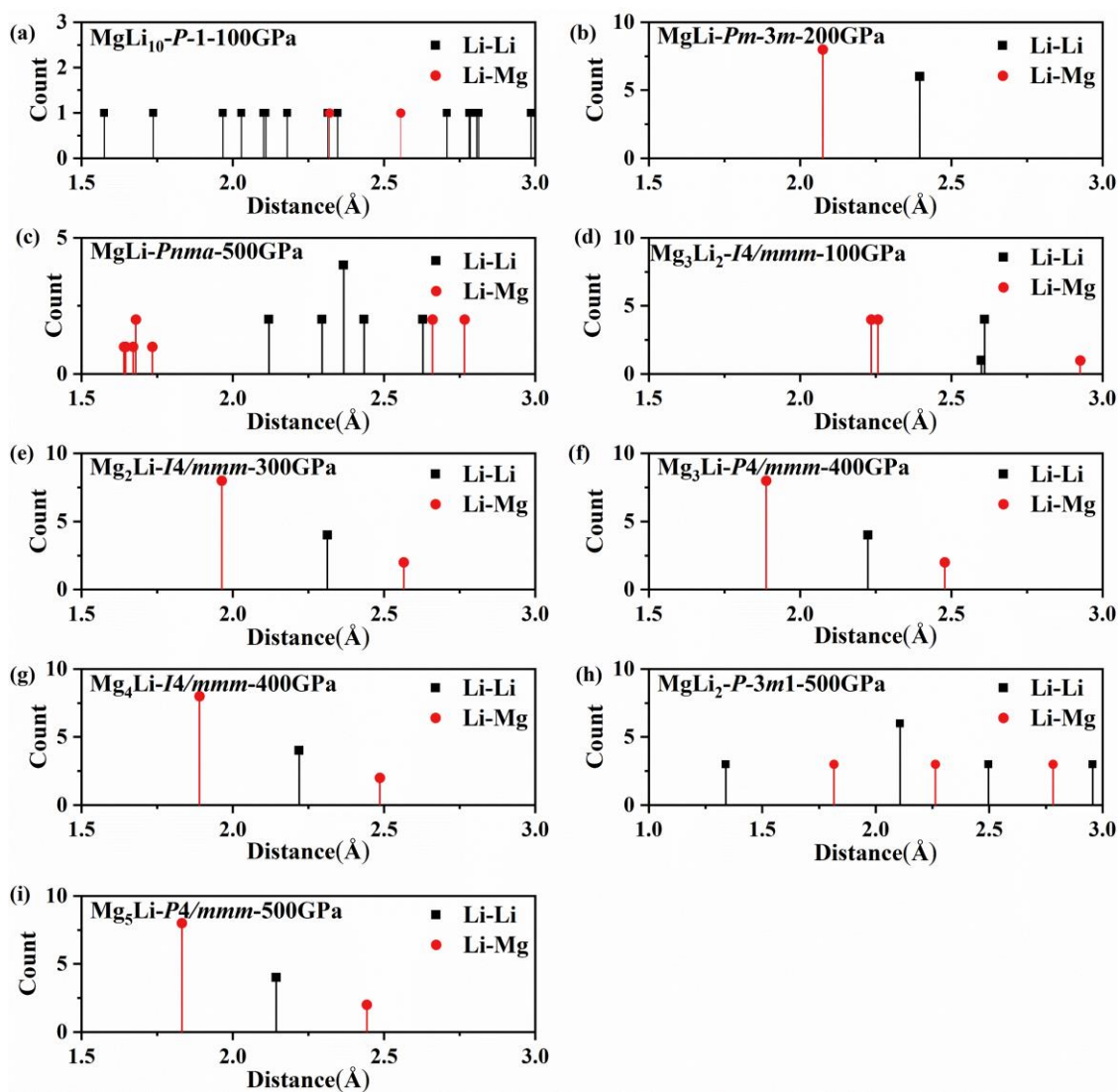


Figure S4. (Color online) Histogram of interatomic separations for (a) $P-1$ $MgLi_{10}$ at 100 GPa; (b) $Pm-3m$ $MgLi$ at 200 GPa; (c) $Pnma$ $MgLi$ at 500 GPa; (d) $I4/mmm$ Mg_3Li_2 at 100 GPa; (e) $I4/mmm$ Mg_2Li at 300 GPa; (f) $P4/mmm$ Mg_3Li at 400 GPa; (g) $I4/mmm$ Mg_4Li at 400 GPa; (h) $P-3m1$ $MgLi_2$ at 500 GPa; (i) $P4/mmm$ Mg_5Li at 500 GPa, respectively. Note that those structures derived from BCC phase (b, d, e-g, i) have similar histogram.

The characteristics of newly predicted structures can be described by their interatomic separation histograms, as shown in Fig. S4. In MgLi_{10} , the coordination numbers of Li atoms vary in the ranges 6–10 with distances from 1.5 Å to 2.5 Å. Li atoms in $\text{MgLi-}Pm-3m$ have coordination number 14, which is similar to bcc-Li. Li atoms in $\text{MgLi-}Pnma$ are connected with six Mg atoms with a separation distance less than 1.75 Å as the nearest neighboring shell; and just above 2 Å, Li atoms coordinate with twelve other Li atoms and four Mg atoms. In Mg_3Li_2 , Li atoms have coordination number 13, they are connected with eight Mg atoms in the nearest shell and five Li atoms in the second shell. The averaged local atomic environment of Li atoms in $\text{Mg}_2\text{Li-}I4/mmm$ is similar to that of $\text{Mg}_3\text{Li-}P4/mmm$ and $\text{Mg}_4\text{Li-}I4/mmm$, it contains a body-centered motif with coordination numbers of Li atoms equal to 8 (cubic coordination).

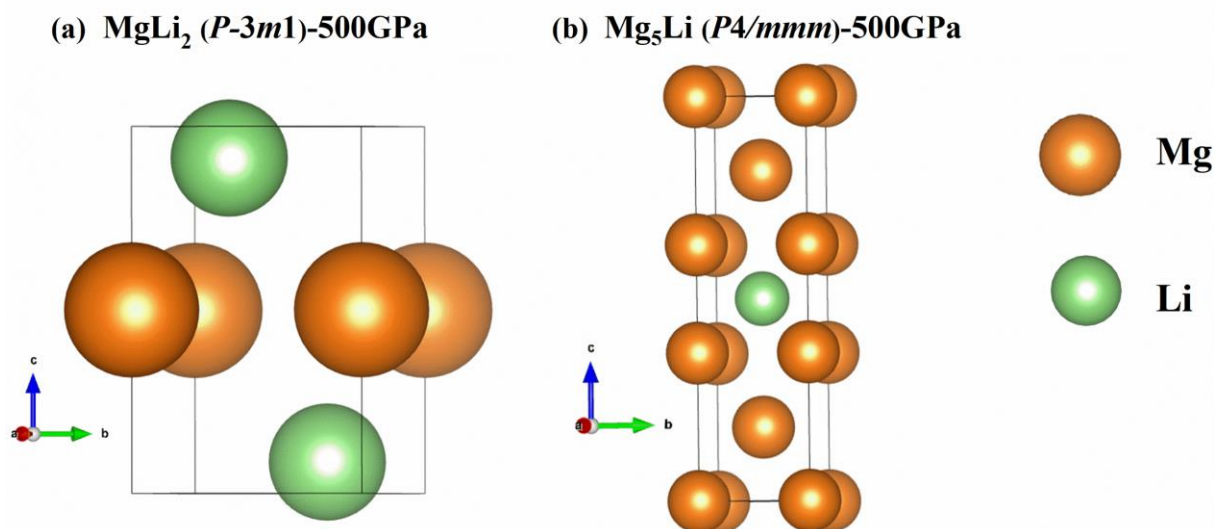


Figure S5. (Color online) (a) Structure of metastable $P-3m1$ MgLi_2 at 500 GPa; (b) Structure of metastable $P4/mmm$ Mg_5Li at 500 GPa; Orange and green spheres represent Mg and Li atoms, respectively.

The new structure MgLi_2 and Mg_5Li are dynamically stable at 170-500 GPa and 0-500 GPa, respectively. As shown in Fig. S5, MgLi_2 is found to be CdI_2 -type² structure (hP3 in the Pearson's symbol) and crystallizes in the trigonal $P-3m1$ space group. As shown in Fig. S4(h),

Li atoms are bonded to three Li atoms and three Mg atoms, the bond lengths for Li-Li and Li-Mg are 1.34 Å and 1.82 Å, respectively. The Li atoms are located at body center and bonded with eight equivalent Mg atoms in $P4/mmm$ Mg₅Li, and the Li-Mg cubic geometry inserted into the two-layer Mg cubic lattice as a guest. The coordination environment is similar to Mg₂Li- $I4/mmm$, and the Li-Li, Li-Mg₁, and Li-Mg₂ bonds are 2.14 Å, 1.83 Å, and 2.44 Å, respectively.

Table S1. Lattice parameters, atomic coordinates and Wyckoff site occupation of $P-1$ MgLi₁₀, $P-3m1$ MgLi₂, $Pm-3m$ MgLi, $Pnma$ MgLi, $I4/mmm$ Mg₃Li₂, $I4/mmm$ Mg₂Li, $P4/mmm$ Mg₃Li, $I4/mmm$ Mg₄Li, and $P4/mmm$ Mg₅Li at the given pressure.

Phase	Lattice parameters (Å)	Atom	Site	Atomic coordinates
$P-1$ MgLi ₁₀ (100 GPa)	$a=4.2731$ $b=4.3904$ $c=4.3942$ $\alpha=87.97^\circ$ $\beta=88.97^\circ$ $\gamma=61.24^\circ$	Li	$1a$	(0.34099 0.88704 0.72062) (0.05131 0.67931 0.88126) (0.76970 0.00255 0.59576) (0.11877 0.23071 0.46101) (0.79363 0.60177 0.44728) (0.39365 0.28971 0.17849) (0.42905 0.37526 0.68948) (0.39605 0.64581 0.32254) (0.49193 0.90920 0.03875) (0.93797 0.92672 0.23680)
		Mg	$1a$	(0.85923 0.33964 0.95506)
$P-3m1$ MgLi ₂ (500 GPa)	$a=b=2.1069$ $c=3.2546$ $\alpha=\beta=90^\circ$ $\gamma=120^\circ$	Li	$2d$	(0.66667 0.33333 0.91395)
		Mg	$1b$	(0.00000 0.00000 0.50000)
$Pm-3m$ MgLi (200 GPa)	$a=b=c=2.395$ 5 $\alpha=\beta=\gamma=90^\circ$	Li	$1b$	(0.50000 0.50000 0.50000)
		Mg	$1a$	(0.00000 0.00000 0.00000)

<i>Pnma</i> MgLi (500 GPa)	$a= 3.3692$ $b= 3.3006$ $c= 3.3146$ $\alpha=\beta=\gamma=90^\circ$	Li	$4c$	(0.30321 0.25000 0.51493)
		Mg	$4c$	(-0.21068 0.25000 0.48872)
<i>I4/mmm</i> Mg ₃ Li ₂ (100 GPa)	$a=b=2.6098$ $c=13.5705$ $\alpha=\beta=\gamma=90^\circ$	Li	$4e$	(0.50000 0.50000 0.09576)
		Mg	$2a$	(0.00000 0.00000 0.00000)
			$4e$	(0.50000 0.50000 0.68865)
<i>I4/mmm</i> Mg ₂ Li (300 GPa)	$a=b=2.3127$ $c=7.3017$ $\alpha=\beta=\gamma=90^\circ$	Li	$2a$	(0.00000 0.00000 0.00000)
		Mg	$4e$	(0.00000 0.00000 0.35126)
<i>P4/mmm</i> Mg ₃ Li (400 GPa)	$a=b=2.2241$ $c=4.9553$ $\alpha=\beta=\gamma=90^\circ$	Li	$1b$	(0.00000 0.00000 0.50000)
		Mg	$1a$	(0.00000 0.00000 0.00000)
			$2h$	(0.50000 0.50000 0.71065)
<i>I4/mmm</i> Mg ₄ Li (400 GPa)	$a=b=2.2196$ $c=12.7959$ $\alpha=\beta=\gamma=90^\circ$	Li	$2a$	(0.50000 0.50000 0.50000)
		Mg	$4e$	(0.50000 0.50000 0.91775)
			$4e$	(0.50000 0.50000 0.30575)
<i>P4/mmm</i> Mg ₅ Li (500 GPa)	$a=b=2.1437$ $c=7.6985$ $\alpha=\beta=\gamma=90^\circ$	Li	$1d$	(0.50000 0.50000 0.50000)
		Mg	$1a$	(0.00000 0.00000 0.00000)
			$2h$	(0.50000 0.50000 0.81727)
		$2g$	(0.00000 0.00000 0.63353)	

Table S2. The valence state of Mg and Li atoms and the Bader charge of ISQs in Mg_mLi_n compounds.

Phase	Mg (per atom)	Li (per atom)	ISQ (e/site)	ISQ(e/cell)
<i>P</i> -1 MgLi ₁₀ (100 GPa)	+0.65	+0.97	/	7.51
<i>Pm</i> -3 <i>m</i> MgLi (200 GPa)	+1.16	+0.6	ISQ1: 0.44; ISQ2: 0.14	1.76
<i>Pnma</i> MgLi (500 GPa)	+1.27	+0.56	0.92	7.32
<i>I4/mmm</i> Mg ₃ Li ₂ (100 GPa)	+1.18	+0.65	ISQ1: 0.55; ISQ2: 0.64 ISQ3: 0.68; ISQ4: 0.50	9.71
<i>I4/mmm</i> Mg ₂ Li (300 GPa)	+1.20	+0.56	ISQ1: 0.64; ISQ2: 0.84 ISQ3: 0.64	5.92
<i>P4/mmm</i> Mg ₃ Li (400 GPa)	+1.20	+0.53	ISQ1: 1.11; ISQ2: 0.89 ISQ3: 0.61	4.11

<i>I4/mmm</i> Mg ₄ Li (400 GPa)	+1.20	+0.53	ISQ1: 1.15; ISQ2: 0.85 ISQ3: 0.61	10.64
--	-------	-------	--------------------------------------	-------

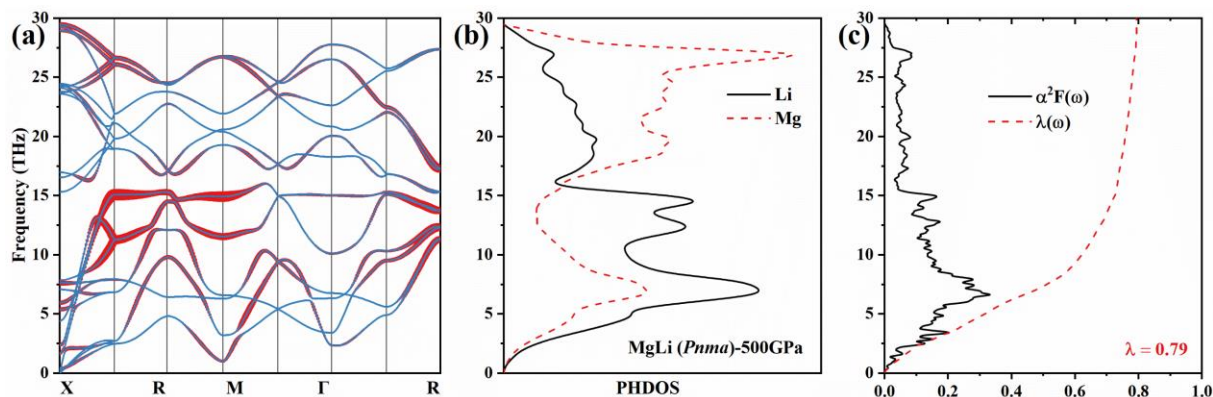


Figure S6. (Color online) (a) Phonon dispersion relations, (b) projected phonon density of states (PHDOS), (c) Eliashberg spectral function $\alpha^2F(\omega)$ and electron-phonon coupling constant λ of *Pnma* MgLi at 500 GPa.

The sizes of the solid red circles are proportional to the electron phonon coupling strength.

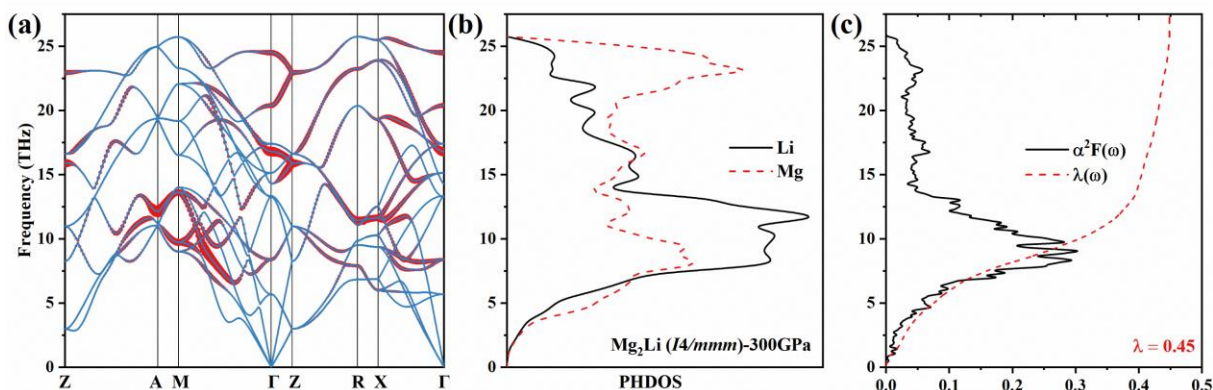


Figure S7. (Color online) (a) Phonon dispersion relations, (b) projected phonon density of states (PHDOS), (c) Eliashberg spectral function $\alpha^2F(\omega)$ and electron-phonon coupling constant λ of *I4/mmm* Mg₂Li at 300 GPa. The sizes of the solid red circles are proportional to the electron-phonon coupling strength.

Figures S6 and S7 show the role of phonon dispersion on superconductivity. The calculated Eliashberg spectral function reflects a 77.7% contribution of phonons below 16 THz to the EPC constant, implying that the superconductivity of the electride MgLi-*Pnma* is dominated by low-frequency phonons. In MgLi-*Pnma*, the calculated EPC parameter (λ) is 0.79, and the

logarithmic average frequency ω_{log} is 176.408, which corresponds to a T_c of 8.91 K. Similarly, the low-frequency phonons below 15 THz play a dominant role in the superconductivity for Mg_2Li , due to their large contribution to λ (78.8%). We conclude that low-frequency phonons jointly contributed by Li and Mg atoms, and the PHDOS of the Li atom is more concentrated at lower frequencies than Mg atoms.

Table S3. The charge state of ISQs and valence electron, q/Q , EPC parameter λ , and superconducting critical temperatures T_c of typical electrides that contain Li.

Phase	q (e/cell)	Q (e/cell)	q/Q	λ	T_c (K)
Li_8Au - Fm - $3m$ -250 GPa	3.0496	76	0.04	2	68.5^3
Li_5N - $P6/mmm$ -150 GPa	1.2475	10	0.12475	1.39	48.97^4
$MgLi$ - Pm - $3m$ -200 GPa	1.76	3	0.58667	1.35	22.8
$Li_{10}Se$ - $C2/m$ -50 GPa	9.8228	32	0.30696	1.28	16^5
Li_8Au - Fm - $3m$ -200 GPa	3.2044	76	0.04216	1.26	51.5^3
Li_5C - $P6/mmm$ -210 GPa	0.5838	9	0.06487	1.26	48.3^6
$LiCa$ - Fd - $3m$ -80 GPa	3.8592	24	0.1608	1.25	18.9^7
Li_6As - $C2/c$ -270 GPa	0.92	44	0.02091	1.2	45.2^8
$Li_{10}Sb$ - $C2/m$ -100 GPa	3.52	30	0.11733	0.8	9.2^8
$MgLi$ - $Pnma$ -500 GPa	7.32	12	0.61	0.79	8.91
$Li_{11}Sb_2$ - $C2/m$ -300 GPa	0.8772	42	0.02089	0.59	9.4^9
Li_8As - $P6/mmm$ -50 GPa	3.27	13	0.25154	0.56	6.3^8
Li - Im - $3m$ -30 GPa	1.4406	2	0.7203	0.51	14^{10}
Li_9Te - $C2/m$ -50 GPa	7.6912	30	0.25637	0.5	4.01^{11}
Li - Im - $3m$ -20.3 GPa	1.4878	2	0.7439	0.49	5.47^{10}
$Li_{10}Te$ - $C2/m$ -100 GPa	3.51	32	0.10969	0.48	4^8
Li - Im - $3m$ -10 GPa	1.5392	2	0.7696	0.47	2.3^{10}
Mg_2Li - $I4/mmm$ -300 GPa	5.92	10	0.592	0.45	3.24

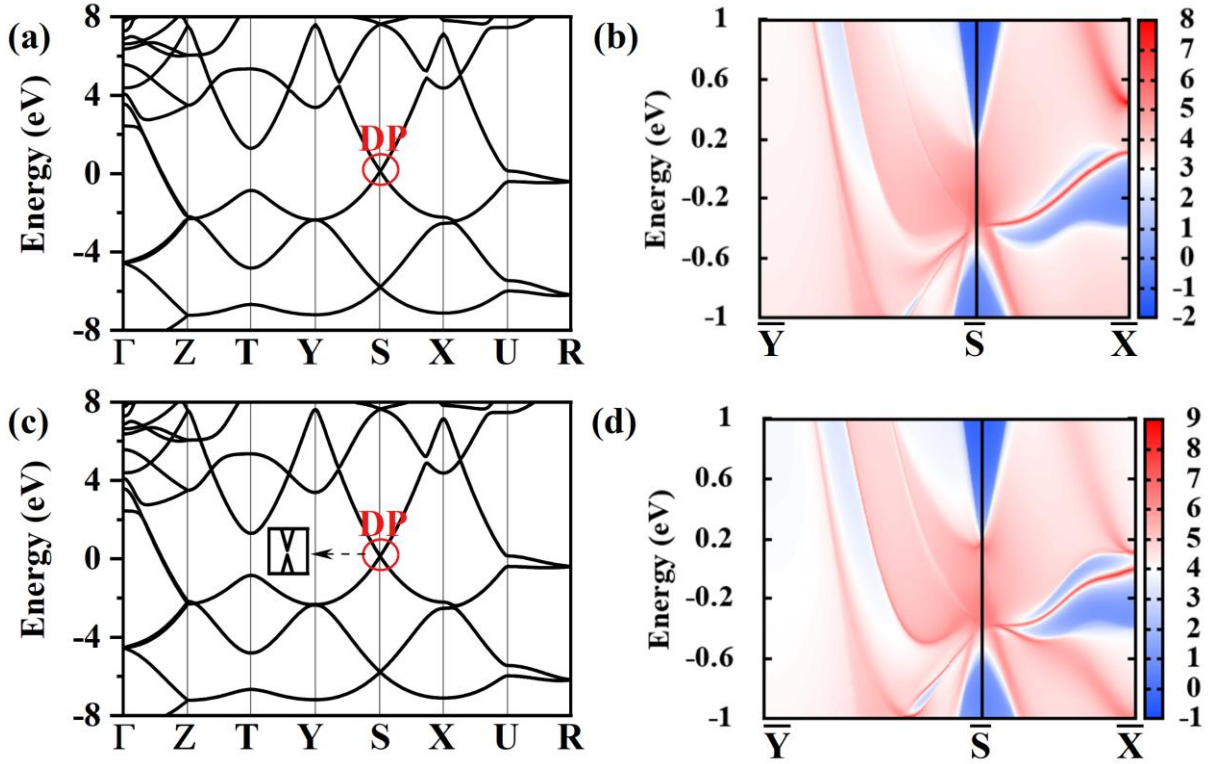


Figure S8. (Color online) (a) Band structure calculated without the SOC effect for MgLi-*Pnma*; (b) Surface states on the (001) surface of MgLi-*Pnma* without the SOC effect; (c) Band structure calculated with the SOC effect for MgLi-*Pnma*, the inset shows a zoomed-in view of the plot of the bands at DP with a gap; (d) Surface states on the (001) surface of MgLi-*Pnma* with the SOC effect; the Fermi level is set to zero. The pressure is 500 GPa.

Table S4. Parity products at TRIMs and the Z_2 Index of MgLi-*Pnma* at 500 GPa.

TRIM	Parity Products	ν	Z_2
Y	-	$\nu_1=0, \nu_1'=1$	
3S	+	$\nu_2=0, \nu_2'=1$	
3X	-	$\nu_3=0, \nu_3'=1$	(1;111)
U	-	$\nu_0=1$	

We report a discovery of nontrivial Z_2 topology in the electronic structures of superconducting electride MgLi-*Pnma*, which is similar to MgLi-*Pm-3m* where the band-crossing point (Dirac point) is located at S points near the Fermi level and gapped with SOC effect. In Table S4 and Fig. S8, we find a topological Z_2 invariant of (1; 111) for the bulk band

and topologically protected surface states in the (001) surfaces, signifying its nontrivial electronic topology.

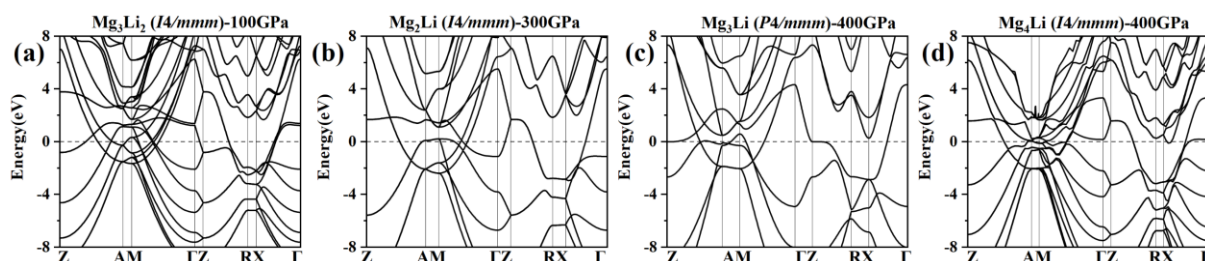


Figure S9. (Color online) Band structures for (a) $I4/mmm$ Mg_3Li_2 at 100 GPa; (b) $I4/mmm$ Mg_2Li at 300 GPa; (c) $P4/mmm$ Mg_3Li at 400 GPa; (d) $I4/mmm$ Mg_4Li at 400 GPa, respectively.

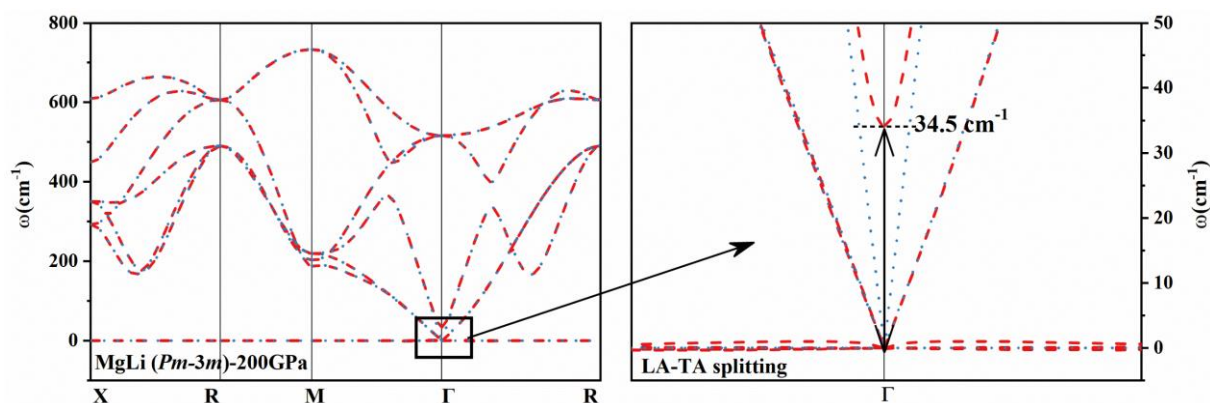


Figure S10. (Color online) Phonon dispersions of $Pm-3m$ $MgLi$ at 200 GPa, which are calculated using Bader charges (dot-dash-ed lines), and compared to that without taking nucleus-ISQ polarization into account (dotted lines in the right panel).

Supplementary references

1. Xu, Y.; Wang, S.; Chen, C.; Li, H.; Zhou, D., Superconductivity at 23 K in $MgLi$ compound at ultrahigh pressure. *Comp. Mater. Sci.* **2019**, *164*, 158-165.
2. Bozorth, R. M., The crystal structure of cadmium iodide. *J. Am. Chem. Soc.* **1922**, *44* (10), 2232-2236.
3. Zhang, X. G.; Yao, Y. S.; Ding, S. C.; Bergara, A.; Li, F.; Liu, Y.; Zhou, X. F.; Yang, G. C., Superconductivity in Li_8Au electride. *Phys. Rev. B* **2023**, *107* (10), L100501.
4. Wan, Z.; Zhang, C.; Yang, T.; Xu, W.; Zhang, R., Predicted superconductivity and superionic state in the electride Li_5N under high pressure. *New J. Phys.* **2022**, *24* (11), 113012.

5. Zhang, X.; Zhao, Y.; Bergara, A.; Yang, G., Superconducting Li_{10}Se electride under pressure. *J. Chem. Phys.* **2022**, *156* (19), 194112.
6. Pereira, Z. S.; Faccin, G. M.; Silva, E. Z. D., Predicted superconductivity in the electride Li_5C . *J. Phys. Chem. C* **2021**, *125* (16), 8899-8906.
7. Xu, Y.; Chen, C.; Wang, S.; Sun, X., Novel structures and superconductivities of calcium–lithium alloys at high pressures: A first-principles study. *J. Alloy. Compd.* **2016**, *669*, 101-107.
8. Zhao, Y.; Bergara, A.; Zhang, X.; Li, F.; Liu, Y.; Yang, G., Interstitial anionic electrons favoring superconductivity in Li-As electrides. *Phys. Rev. B* **2023**, *108* (10), 104505.
9. Zhao, Y.; Gao, J.; Zhang, X.; Ding, S.; Liu, Y.; Yang, G., Superconducting $\text{Li}_{11}\text{Sb}_2$ electride at ambient pressure. *J. Mater. Chem. C* **2023**, *11* (48), 17087-17092.
10. Shi, L.; Papaconstantopoulos, D. A., Theoretical predictions of superconductivity in alkali metals under high pressure. *Phys. Rev. B* **2006**, *73* (18), 184516.
11. Zhang, X.; Li, F.; Bergara, A.; Yang, G., Pressure-induced superconductivity in Li-Te electrides. *Phys. Rev. B* **2021**, *104* (13), 134505.